Karlsruhe Institute of Technology

Characterization of the October 2017 Wildfires in Portugal and Spain and Their Long-Range Aerosol Impacts Using Remote Sensing and Atmospheric Modeling

Master's Thesis of

Dorsa Amini

At KIT
Institut für Meteorologie und Klimaforschung Atmosphärische Spurengase und Fernerkundung (IMKASF)

First examiner: Prof. Dr. Jan Cermak
First advisor: Dr. Gholamali Hoshyaripour
Second advisor: Dr. rer. nat. Eva Pauli

01. September 2025 – 27. March 2026

Characterization of the October 2017 Wildfires in Portugal and Spain and Their Long-Range Aerosol Impacts Using Remote Sensing and Atmospheric Modeling (Master's Thesis) I declare that I have developed and written the enclosed thesis completely by myself. I have not used any other than the aids that I have mentioned. I have marked all parts of the thesis that I have included from referenced literature, either in their original wording or paraphrasing their contents. I have followed the by-laws to implement scientific integrity at KIT.

Karlsruhe, 27. March 2026

(Dorsa Amini)

Abstract

Wildfires emit large amounts of aerosols that can be transported over long distances and interact with radiation and clouds, yet their representation in atmospheric models remains uncertain. This thesis investigates the October 2017 Iberian wildfires, one of the most extreme fire episodes in recent European history, using the ICOsahedral Nonhydrostatic model with Aerosols and Reactive Trace gases (ICON-ART) model together with satellite observations. The study evaluates the model's ability to simulate the injection height, long-range transport, and vertical distribution of the smoke plume, and examines the potential downwind impacts on aerosol–cloud interactions.

ICON-ART simulations were performed with different configurations, including variations in the scaling of the additional sensible heat release from fires and the activation of Aerosol–Radiation Interactions (ARI). Model results were compared with Aerosol Optical Depth (AOD) from the Multi Angle Implementation of Atmospheric Correction (MAIAC) algorithm, attenuated backscatter profiles from the Cloud–Aerosol Lidar and Infrared Pathfinder Satellite Observation (CALIPSO) lidar, and cloud properties from Moderate Resolution Imaging Spectroradiometer (MODIS). A regime-based statistical analysis was used to investigate the relationship between simulated soot AOD and observed cloud fraction, classifying pixels into four categories based on aerosol loading and cloud cover.

The comparison shows that ICON-ART realistically captures the horizontal transport of the plume across Europe and reproduces its elevated vertical structure, with injection heights reaching 8–11 km. Sensitivity experiments demonstrate that both the plume-rise scaling and aerosol–radiation interactions influence the vertical extent and coherence of the simulated smoke layer. However, the statistical analysis reveals only a weak correlation between AOD and cloud fraction. The most striking finding is the extremely limited spatial overlap between heavy smoke (AOD ≥ 0.4) and extensive cloud cover (cloud fraction ≥ 0.8) - a combination defined as the polluted-cloudy regime. On 17 October 2017, less than 4% of the analysed pixels fall into this regime, and the correlation is negligible. This pattern is confirmed for 18 October. Geometric analysis further shows that the smoke plume is predominantly elevated and often located in regions where clouds occur at different altitudes and phases (e.g., warm low-level clouds versus cold ice clouds), limiting direct aerosol–cloud interactions.

These results demonstrate that column-integrated AOD alone is an insufficient proxy for aerosol–cloud interactions in the case of elevated smoke plumes. Instead, vertically resolved information and the geometric overlap between aerosol and cloud layers are essential. The findings highlight the value of combining active lidar observations with online-coupled models like ICON-ART to diagnose the conditions under which wildfire smoke can affect

clouds. This thesis contributes to a better understanding of the atmospheric impacts of extreme wildfire events and provides a framework for future observational and modeling studies.

Zusammenfassung

Waldbrände setzen große Mengen an Aerosolen frei, die über weite Strecken transportiert werden und mit Strahlung und Wolken interagieren können. Ihre Abbildung in Atmosphärenmodellen ist jedoch nach wie vor mit Unsicherheiten behaftet. Diese Arbeit untersucht die iberischen Waldbrände vom Oktober 2017, eines der extremsten Brandereignisse der jüngeren europäischen Geschichte, mithilfe des ICOsahedral Nonhydrostatic modell mit dem Äerosols and Reactive Trace gases"Modul ICON-ART in Kombination mit Satellitenbeobachtungen. Die Studie bewertet die Fähigkeit des Modells, die Injektionshöhe, den Ferntransport und die vertikale Verteilung der Rauchfahne zu simulieren, und untersucht die potenziellen Auswirkungen auf Aerosol-Wolken-Wechselwirkungen in den Abwindregionen.

Es wurden ICON-ART-Simulationen mit verschiedenen Konfigurationen durchgeführt, darunter Variationen der Skalierung der zusätzlichen sensiblen Wärmefreisetzung durch Brände und die Aktivierung von Aerosol-Strahlungs-Wechselwirkungen (Aerosol–Radiation Interactions, ARI). Die Modellergebnisse wurden mit der Aerosoloptischen Dicke (Aerosol Optical Depth, AOD) aus dem Multi-Angle Implementation of Atmospheric Correction (MAIAC)-Algorithmus, abgeschwächten Rückstreuprofilen des Cloud-Aerosol Lidar and Infrared Pathfinder Satellite Observation (CALIPSO)-Lidars sowie Wolkeneigenschaften des Moderate Resolution Imaging Spectroradiometer (MODIS) verglichen. Mithilfe einer regimebasierten statistischen Analyse wurde der Zusammenhang zwischen simulierter Ruß-AOD und beobachtetem Wolkenanteil untersucht.

Der Vergleich zeigt, dass ICON-ART den horizontalen Transport der Rauchfahne über Europa realistisch abbildet und deren erhöhte vertikale Struktur mit Injektionshöhen von 8–11 km reproduziert. Sensitivitätsexperimente belegen, dass sowohl die Parametrisierung des Aufstiegs der Rauchfahne als auch die Aerosol-Strahlungs-Wechselwirkungen die vertikale Ausdehnung und Kohärenz der simulierten Rauchschicht beeinflussen. Die statistische Analyse ergibt jedoch nur eine schwache Korrelation zwischen AOD und Wolkenanteil.Besonders auffällig ist die äußerst geringe räumliche Überlappung zwischen starkem Rauch (AOD $\geq 0{,}4$) und ausgedehnter Bewölkung (Wolkenanteil $\geq 0{,}8$), eine Kombination, die als "verschmutzt-bewölktes Regime"definiert wird. Am 17. Oktober 2017 fielen weniger als 4% der analysierten Pixel in das Regime "verschmutzt–bewölkt", und die Korrelation in diesem Regime ist vernachlässigbar. Dieses Muster bestätigt sich für den 18. Oktober. Die geometrische Analyse zeigt zudem, dass die Rauchfahne vorwiegend in der Höhe liegt und sich oft in Regionen befindet, in denen Wolken in unterschiedlichen Höhen und Phasen auftreten (z. B. warme, tiefliegende Wolken im Vergleich zu kalten Eiswolken), was direkte Aerosol-Wolken-Wechselwirkungen einschränkt und ihre Analyse erschwert.

Diese Ergebnisse belegen, dass die säulenintegrierte AOD allein kein ausreichender Indikator für Aerosol-Wolken-Wechselwirkungen bei hochliegenden Rauchfahnen ist. Stattdessen sind vertikal aufgelöste Informationen und die geometrische Überlappung zwischen Aerosol- und Wolkenschichten unerlässlich. Die Erkenntnisse unterstreichen den Wert der Kombination von aktiven Lidarmessungen mit online-gekoppelten Modellen wie ICON-ART, um die Bedingungen zu identifizieren, unter denen Waldbrandrauch Wolken beeinflussen kann. Diese Arbeit trägt zu einem besseren Verständnis der atmosphärischen Auswirkungen extremer Waldbrände bei und liefert einen Rahmen für zukünftige Beobachtungs- und Modellierungsstudien.

Preface

ChatGPT (`https://chatgpt.com/`) was used as a tool to correct grammatical errors and improve language clarity. It was also used for translating the German abstract. Initial spell checking was performed using Writefull (`https://www.writefull.com/`).

Special thanks to the German Climate Computing Centre (German Climate Computing Centre (DKRZ)) for providing computing and storage resources.

Contents

List of Figures

List of Tables

Abbreviations

ACI Aerosol–Cloud Interactions.

AOD Aerosol Optical Depth.

ARI Aerosol–Radiation Interactions.

BB Biomass Burning.

BC Black Carbon.

C2SM Center for Climate Systems Modeling.

CALIOP Cloud–Aerosol Lidar with Orthogonal Polarization.

CALIPSO Cloud–Aerosol Lidar and Infrared Pathfinder Satellite Observation.

CCN Cloud Condensation Nuclei.

DKRZ German Climate Computing Centre.

DWD German Weather Service (Deutscher Wetterdienst).

FRP Fire Radiative Power.

GFAS Global Fire Assimilation System.

ICON ICOsahedral Nonhydrostatic Model.

ICON-ART ICOsahedral Nonhydrostatic model with Aerosols and Reactive Trace gases.

MAIAC Multi Angle Implementation of Atmospheric Correction.

MODIS Moderate Resolution Imaging Spectroradiometer.

NDVI Normalized Difference Vegetation Index.

NWP Numerical weather prediction.

OC Organic Carbon.

1 Introduction

Atmospheric aerosol particles are tiny solid or liquid substances suspended in air, originating from both natural sources such as dust storms, volcanic eruptions and industrial emissions [Intergovernmental Panel on Climate Change (IPCC), 2021]. Among these sources, wildfires are particularly important because they release vast amounts of aerosols over short periods and can inject them high into the atmosphere, where they may be transported across continents and affect air quality, radiation, and cloud formation in downwind regions. The atmospheric relevance of aerosols arises from their ability to interact with radiation and clouds through Aerosol-Radiation Interactions (ARI) and Aerosol–Cloud Interactions (ACI) [López-Romero et al., 2021], yet despite decades of research, their net effect on the climate system remains one of the largest uncertainties [Intergovernmental Panel on Climate Change (IPCC), 2021]. Against this backdrop, climate change is projected to intensify wildfire activity in many regions: increasing summer aridity dries vegetation, creating conditions conducive to larger and more severe fires [Grünig et al., 2023]. Extreme wildfire events are expected to become more frequent, with wildfires emerging as the disturbance agent most sensitive to climate change in European forests [Grünig et al., 2026]. Increasing wildfire activity can have substantial ecological and societal impacts, including risks to human health, infrastructure, and ecosystem services [Grünig et al., 2023]. Understanding how wildfire smoke is transported during individual events and how it interacts with radiation and clouds on short time scales is therefore not only scientific challenge but also a societal priority.

1.1 Aerosol Interactions with Radiation and Clouds

Aerosols influence the climate system through three main pathways: direct radiative effects, the semi-direct effect, and indirect radiative effects [Intergovernmental Panel on Climate Change (IPCC), 2021, Boucher et al., 2013]. Direct effects refer to the scattering and absorption of radiation by aerosol particles, which can either cool or warm the atmosphere depending on aerosol composition [Boucher, 2015, Bond et al., 2013]. Absorbing aerosols such as Black Carbon (BC) can additionally modify atmospheric stability through the semi-direct effect, where heating of the aerosol layer affects cloud cover and temperature profiles [Tegen and Heinold, 2018, Koch and Del Genio, 2010]. Finally, indirect effects arise from aerosol–cloud interactions: aerosols act as cloud condensation nuclei, altering cloud microphysics, albedo, and lifetime — processes known as the Twomey and Albrecht effects [Twomey, 1974, Albrecht, 1989]. Together, these pathways represent the largest source of uncertainty in current estimates of anthropogenic radiative forcing [Boucher et al., 2013].

1.2 Biomass Burning as an Aerosol Source

Biomass Burning (BB) is a major episodic source of carbonaceous aerosols, contributing substantially to fine-mode organic aerosol and black carbon on global scales [Crutzen and Andreae, 1990, Akagi et al., 2011]. Emissions originate from wildfires, agricultural burning, and prescribed fires, and are particularly prevalent in tropical regions during the dry season [Andreae, 2001]. Biomass burning is thought to be the largest source of primary fine carbonaceous particles worldwide [Akagi et al., 2011]. However, it is also highly relevant for Europe, where wildfires in the Iberian Peninsula and Eastern Europe contribute substantially to regional aerosol loadings [Broda et al., 2025].

The particles emitted by biomass burning strongly influence both ARI and ACI. Black carbon absorbs solar radiation, while organic aerosols can scatter or, in the case of brown carbon, also absorb at shorter wavelengths [Andreae and Gelencsér, 2006]. A significant fraction of biomass burning organic aerosol is water-soluble, enhancing its ability to act as CCN and therefore its potential to modify cloud properties [Akagi et al., 2011]. During transport, these plumes undergo complex transformations that modify their optical properties and CCN activity [Palm et al., 2020, Ohneiser et al., 2023].

Unlike continuous anthropogenic emissions, wildfires are episodic and generate intense heat fluxes that drive strong fire-induced convection. As a result, smoke can be injected well above the planetary boundary layer, sometimes reaching the upper troposphere through pyroconvective processes [Rémy et al., 2017, Fromm et al., 2010, Peterson et al., 2018]. This vertical redistribution fundamentally alters subsequent transport, lifetime, and climate impacts of the emitted aerosols.

1.3 The Importance of Injection Height

The injection height of smoke is a critical parameter controlling long-range transport, atmospheric lifetime, and vertical overlap with cloud layers [Textor et al., 2006]. Aerosols released above the boundary layer are no longer subject to rapid removal by dry deposition and boundary-layer turbulent mixing. Instead, they can be transported over thousands of kilometers, remaining in the atmosphere for days to weeks [Zavala et al., 2009]. Whether smoke is emitted below or above the planetary boundary layer top therefore has profound consequences for downwind air quality, radiation, and cloud interactions. Because most global and regional models cannot explicitly resolve fire-induced convection, they rely on specialized parametrization to estimate injection heights [Freitas et al., 2006, Grell et al., 2011]. Uncertainties in these estimates propagate directly into simulated aerosol transport, radiative effects, aerosol-cloud interactions in downwind regions.

1.4 The October 2017 Iberian Wildfires

The October 2017 wildfires in Portugal and northern Spain represent one of the most extreme fire events in recent European history. Between 15 and 17 October, hundreds of fires burned across the region, consuming more than 200,000 ha in Portugal alone and an additional 42,000 ha in Galicia, Spain [Ramos et al., 2023, Chas-Amil et al., 2020]. The fires occurred under exceptional meteorological conditions, combining a severe drought with the passage of ex-hurricane Ophelia along the Iberian coast, which generated extreme fire weather [Augusto et al., 2020, Turco et al., 2019]. The resulting smoke plumes were injected into the upper troposphere and transported across Western Europe, affecting regions as far as Germany and producing a unique "red sky" phenomenon over the United Kingdom [Peterson et al., 2018, Wyche et al., 2022].

1.5 Research Gap and Motivation

Despite advances in remote sensing and modeling, substantial uncertainties remain in representing wildfire plume injection heights, vertical distribution, and the resulting downwind aerosol impacts over Europe. In particular, consistent evaluation of modeled plume structure against satellite-derived horizontal and vertical observations remains limited for intense midlatitude fire episodes. Many previous studies have focused on tropical biomass burning or on the Southeast Atlantic stratocumulus region, where smoke–cloud interactions are persistent and well-documented [Adebiyi et al., 2015, Diamond et al., 2022]. However, extreme extratropical events such as the October 2017 Iberian wildfires are less frequently examined, and the performance of online-coupled models like ICON-ART in simulating such events has not been comprehensively assessed.

The combination of intense fire emissions, exceptional meteorological forcing, and long-range transport across a continent offers a unique opportunity to evaluate the processes that control the fate of wildfire smoke and its interactions with radiation and clouds. The October 2017 event therefore provides a valuable case study to assess model performance in simulating plume rise, long-range transport, and potential aerosol–cloud interactions under extreme meteorological conditions.

1.6 Study Objectives and Approach

This thesis aims to evaluate the ability of the ICOsahedral Nonhydrostatic model with Aerosols and Reactive Trace gases (ICON-ART) to simulate wildfire plume dynamics and to assess the downwind impacts of smoke aerosols on radiation and clouds. To achieve this, the study integrates satellite observations and atmospheric modeling to characterize the October 2017 Iberian wildfires and their long-range transport across Europe.

Aerosol optical depth and cloud properties are derived from the Moderate Resolution Imaging Spectroradiometer MODIS using MAIAC algorithm, which provides high-resolution retrievals suitable for capturing plume structure [Lyapustin et al., 2018]. The vertical structure of smoke plumes is constrained using lidar observations from the Cloud-Aerosol Lidar and Infrared Pathfinder Satellite Observation CALIPSO mission [Winker et al., 2009]. These observations provide both horizontal and vertical constraints on the aerosol distribution.

For process-based analysis, the ICON-ART model is employed. ICON-ART is a weather and climate model that simulates meteorology, fire emissions including plume rise, aerosol transport, and aerosol–radiation interactions in a fully consistent manner [Rieger et al., 2015, Schröter et al., 2018, Hoshyaripour et al., 2025]. Sensitivity experiments are performed to investigate the influence of aerosol–radiation interactions and the fire intensity scaling factor on simulated plume height and transport.

1.7 Research Questions

This thesis addresses the following research questions:

1. How accurately can ICON-ART simulate the injection height, long-range transport, and vertical distribution of aerosols emitted during the October 2017 wildfires when evaluated against MODIS and Cloud–Aerosol Lidar with Orthogonal Polarization (CALIOP) observations?
2. To what extent did the transported smoke plume influence radiative conditions and aerosol–cloud interactions over downwind regions such as Germany?

Based on the current understanding of wildfire plume dynamics and aerosol processes, the following hypotheses are tested:

1. The ICON-ART model is able to realistically reproduce the injection height, vertical structure, and long-range transport of the smoke plume emitted during the October 2017 Iberian wildfires when compared with satellite observations.
2. The transported wildfire aerosol plume influences the radiative environment and cloud properties over downwind regions such as Germany through two main pathways: (1) by acting as cloud condensation nuclei (aerosol–cloud interactions, ACI), which may increase cloud droplet number concentration and cloud fraction; and (2) by absorbing solar radiation (aerosol–radiation interactions, ARI), which heats the atmosphere and can affect cloud development via the semi-direct effect.

1.8 Thesis Outline

The thesis is structured as follows. Chapter 2 provides the theoretical background on aerosol properties, aerosol–radiation and aerosol–cloud interactions, wildfire emissions,

plume dynamics, and long-range transport. Chapter 3 describes the October 2017 Iberian wildfire event in detail, including the meteorological context, drought preconditioning, fire weather indices, emissions, and downwind effects. Chapter 4 presents the data and methods, including satellite products, the ICON-ART model configuration, simulation setup, and analysis techniques. Chapter 5 presents the results of model evaluation, comparing simulated aerosol fields with MAIAC and CALIPSO observations. Chapter 6 discusses these findings in the context of existing literature and interprets their implications. Chapter 7 summarizes the main findings, answers the research questions, and outlines directions for future research.

2 Theoretical background

This chapter provides the theoretical foundation necessary to interpret the observational and modeling results presented in this thesis. It introduces the fundamental concepts related to atmospheric aerosols, their sources and properties, and their interactions with radiation and clouds. The chapter is structured into two main parts: Section 2.1 covers general aerosol science applicable to all aerosol types, while Section 2.2 focuses specifically on wildfires as a source of aerosols and their unique interactions with the atmosphere. These concepts form the basis for the subsequent analysis of the October 2017 wildfire event using satellite observations and regional atmospheric modeling.

2.1 Aerosols

2.1.1 Aerosol–Radiation Interactions

Aerosol-radiation interactions encompass the direct, semi-direct, and indirect effects of aerosols on Earth's energy balance. A conceptual overview of the different pathways through which aerosols influence radiation and clouds is shown in Fig. 2.1. This section focuses on direct and semi-direct effects, while indirect effects (aerosol-cloud interactions) are discussed in Section 2.1.2.

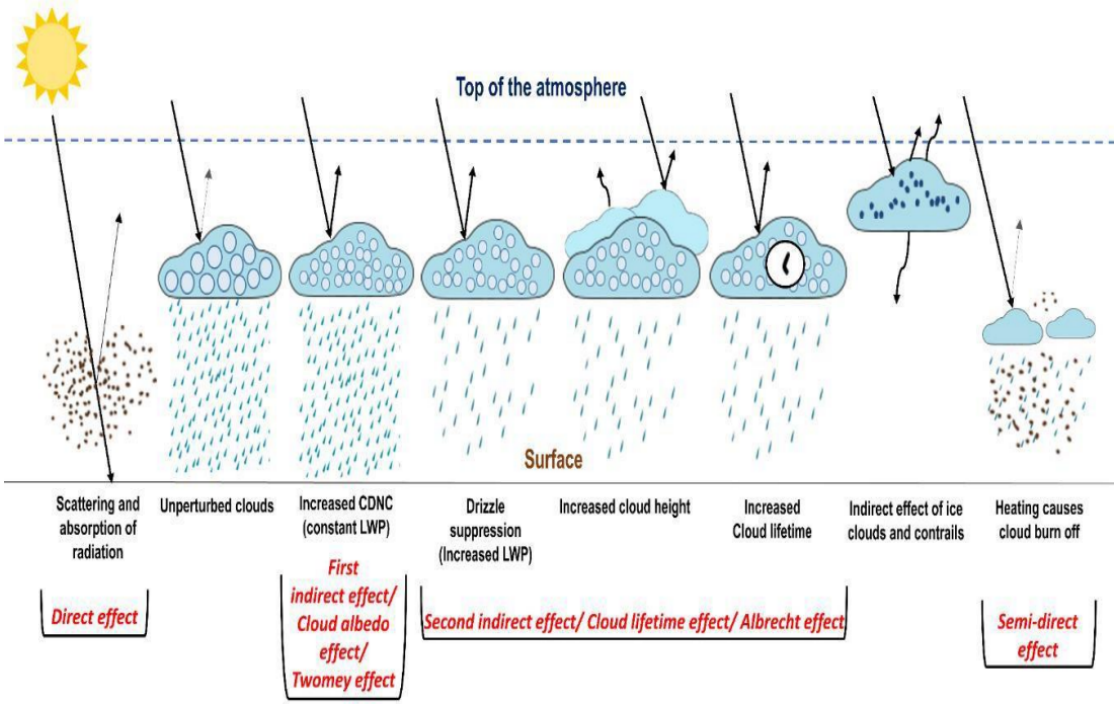

Figure 2.1: Conceptual illustration of the main aerosol radiative effects. Aerosols influence the Earth's radiation budget through three primary mechanisms: (1) the **direct effect**, where aerosol particles scatter and absorb incoming solar radiation; (2) the **first and second indirect effects**, where aerosols act as cloud condensation nuclei and modify cloud droplet number concentration, cloud albedo (Twomey effect), and cloud lifetime (Albrecht effect); and (3) the **semi-direct effect**, where absorption of solar radiation by aerosols heats the atmosphere and can modify cloud cover and stability. Adapted from Panda et al. [2023].

2.1.1.1 Optical Properties

To quantitatively describe aerosol-radiation interactions, three key optical properties are commonly used [Boucher, 2015]. The first is the **mass extinction coefficient**, which quantifies the total attenuation of radiation by aerosols per unit mass — that is, the combined effect of scattering and absorption. The second is the **single scattering albedo**, defined as the ratio of scattering to extinction (scattering + absorption). This dimensionless parameter indicates the fraction of radiation that is scattered versus absorbed, with values close to 1 for purely scattering aerosols (e.g., sulfate) and lower values for absorbing aerosols (e.g., black carbon). The third is the **asymmetry parameter**, which describes the angular distribution of scattered radiation. It ranges from -1 for completely backscattered to +1 for completely forward scattered radiation, with most atmospheric aerosols exhibiting strong forward scattering (values typically between 0.6 and 0.8) [Hess et al., 1998]. These properties vary with aerosol composition, size distribution, and morphology, and determine how a given aerosol population affects the radiative balance at the surface, within the atmosphere, and at the top of the atmosphere.

2.1.1.2 Direct Radiative Effects

Aerosols influence Earth's weather and climate by interacting directly with solar and terrestrial radiation. Some particles mainly scatter sunlight back to space, while others absorb radiation within the atmosphere. Scattering aerosols, such as sulfate particles, generally lead to a cooling effect at the surface and top of atmosphere. Absorbing aerosols, especially black carbon, warm the atmospheric layer in which they are located while simultaneously reducing surface solar radiation - a phenomenon referred to as surface dimming [Boucher, 2015]. The overall radiative effect depends on aerosol composition, size distribution, mixing state, and surface albedo [O'Donnell, 2010]. The balance between scattering and absorbing components determines whether an aerosol population exerts a net cooling or warming influence.

2.1.1.3 Semi-Direct Effect

In addition to direct radiative effects, absorbing aerosols can modify atmospheric stability through the semi-direct effect. Heating of the aerosol layer by absorption of solar radiation can evaporate clouds, reduce cloud cover, and alter temperature profiles, which in turn affects atmospheric dynamics and precipitation [Tegen and Heinold, 2018, Koch and Del Genio, 2010]. This effect bridges the gap between aerosol-radiation and aerosol-cloud interactions, as absorption modulates cloud properties without requiring aerosols to act as cloud condensation nuclei.

Clouds themselves play a key role in modulating aerosol-radiation interactions. In cloudy conditions, the presence of clouds can partially mask aerosol effects, since clouds reflect a large fraction of incoming solar radiation. However, if an absorbing aerosol layer is located above clouds, it can absorb radiation that would otherwise be reflected back to space, leading to a net warming effect at the top of the atmosphere [Andersen, 2017, Chand et al., 2009].

On a global average, aerosols exert a net cooling effect on the climate system, partly offsetting greenhouse gas-induced warming. However, the magnitude and even the sign of aerosol radiative forcing vary strongly across regions and depend on aerosol type, cloud cover, and surface properties. These complexities make aerosol-radiation interactions one of the largest sources of uncertainty in current climate assessments.

2.1.2 Aerosol–Cloud Interactions

Aerosol–Cloud Interactions (ACI), also referred to as indirect radiative effects, arise because aerosols act as Cloud Condensation Nuclei (CCN) or ice nucleating particles, thereby modifying cloud microphysical properties. An increase in aerosol concentration generally increases cloud droplet number concentration while reducing mean droplet size - an effect first described by Twomey [1974] and now known as the Twomey effect (or first indirect effect). For a fixed liquid water content, clouds composed of smaller, more numerous droplets have higher albedo, enhancing the reflection of solar radiation back to space.

Beyond this immediate radiative impact, aerosol-induced changes in droplet size can suppress warm rain formation, as smaller droplets coalesce less efficiently [Albrecht, 1989]. This may prolong cloud lifetime, increase cloud thickness, and alter cloud fractional cover, processes collectively referred to as the Albrecht effect (or second indirect effect). Aerosol effects on ice clouds and mixed-phase clouds are even more complex and remain poorly constrained [Boucher et al., 2013].

Together with direct and semi-direct effects, these indirect radiative effects constitute the largest source of uncertainty in current estimates of anthropogenic radiative forcing [Boucher et al., 2013].

2.2 Wildfires

2.2.1 Wildfire Emissions and Aerosol Properties

Wildfires represent an important and highly variable source of atmospheric aerosols. They belong to the broader category of biomass burning, which also includes agricultural burning, prescribed fires, and domestic biofuel combustion for cooking and heating [Akagi et al., 2011]. Unlike managed fires, wildfires occur largely without direct human control and are strongly shaped by environmental conditions. As a result, wildfire emissions are episodic and difficult to predict in space and time [Akagi et al., 2011].

The amount and type of material released during a wildfire depend on how the fire develops. Fire intensity and combustion conditions vary with fuel availability, fuel moisture, and meteorological factors such as temperature, humidity, and wind. Two primary combustion regimes can be distinguished:

- **Flaming combustion**: Occurs at high temperatures and favors the production of black carbon through efficient, high-temperature burning.
- **Smoldering combustion**: Occurs at lower temperatures and releases larger amounts of organic aerosols and trace gases through incomplete combustion.

These different regimes occur simultaneously within a fire, producing a mixture of combustion products that evolve as the fire progresses.

Wildfire smoke consists mainly of carbon-containing particles, primarily black carbon (BC) and organic carbon (OC). The ratio of organic carbon to black carbon (OC/BC) varies widely depending on vegetation type and combustion conditions, ranging from approximately 4:1 in savanna fires to 15:1 in temperate forest fires [Akagi et al., 2011]. This means that BC typically accounts for 6-19% of the carbonaceous aerosol mass, while OC constitutes the remaining 81-94%. Particle sizes typically range from freshly emitted accumulation mode particles (0.1-1 μm) to larger supermicron particles, with the fine fraction dominating the aerosol mass and being most relevant for long-range transport and radiative effects.

The optical properties of biomass burning aerosols are strongly correlated with particle size and BC content [Reid et al., 2005]. Based on a compilation of measurements, Reid et al. [2005] recommend a representative mass absorption coefficient of 0.50 ± 0.15 m^2 g^{-1} and a single scattering albedo of 0.89 at 550 nm for fresh smoke, though individual fires can deviate considerably from these averages. During transport, biomass burning plumes undergo complex physical and chemical transformations, including evaporation of semi-volatile components, condensation of secondary organic aerosol, and changes in mixing state. These aging processes modify the optical properties and CCN activity of the aerosol [Palm et al., 2020, Ohneiser et al., 2023]. Despite these efforts to characterize biomass burning aerosols, Brown et al. [2021] found that current representations in many climate models are still too absorbing compared to observations, highlighting remaining uncertainties.

The particles emitted by wildfires strongly influence both aerosol-radiation and aerosol-cloud interactions. Black carbon absorbs solar radiation, contributing to positive radiative forcing, while organic aerosols can scatter or, in the case of brown carbon, also absorb at ultraviolet and visible wavelengths [Andreae and Gelencsér, 2006]. A significant fraction of biomass burning organic aerosol is water-soluble, enhancing its ability to act as CCN and therefore its potential to modify cloud properties [Akagi et al., 2011].

2.2.2 Wildfire–Atmosphere Interactions

Wildfires modify the atmosphere primarily through the large amounts of heat they release over short periods. This heat creates strong upward motion - a process known as **pyroconvection** — and disturbs the surrounding airflow, causing air from the environment to be drawn toward the fire and redistributed vertically. Pyroconvection can range from small-scale turbulent plumes to deep convective clouds (pyrocumulus and pyrocumulonimbus) that inject smoke into the upper troposphere or even lower stratosphere.

Meteorological conditions play a critical role in determining fire behavior. The term **fire weather** refers to atmospheric conditions that promote fire ignition and spread, typically characterized by high temperatures, low relative humidity, strong winds, and the absence of precipitation [Goodrick et al., 2017]. High temperatures pre heat fuels and reduce their moisture content, while low relative humidity dries vegetation and increases flammability. Strong winds supply oxygen, drive rapid fire spread, and can transport embers ahead of the fire front, creating new ignition sources. The absence of precipitation means no moisture is available to suppress fire activity. Extreme combinations of these factors create conditions conducive to uncontrollable wildfires.

As the fire evolves, these disturbances change continuously, leading to highly variable wind and turbulence patterns near the surface and within the lower atmosphere. Key processes illustrated in Figure 2.2 include:

- **Buoyancy**: The heat released by the fire warms the surrounding air, reducing its density and causing it to rise. The strength of buoyancy determines the initial upward acceleration of the smoke plume.

- **Entrainment**: As the plume rises, it mixes with surrounding air, entraining cooler ambient air into the plume. This dilutes the smoke and affects plume temperature and momentum.
- **Ambient stratification**: The stability of the surrounding atmosphere (temperature profile) can either inhibit or enhance vertical plume development. A stable layer can act as a lid, trapping smoke near the surface, while unstable conditions promote deep convection.

At the same time, the altered atmospheric flow feeds back on the fire by influencing how energy is supplied to the flame and how emissions are carried away. Because of this mutual influence, wildfire behavior and atmospheric dynamics cannot be treated as independent processes; instead, they form an interacting system in which fire-driven motions control plume formation and determine how smoke initially enters the atmosphere [Desai et al., 2024, Linn et al., 2025].

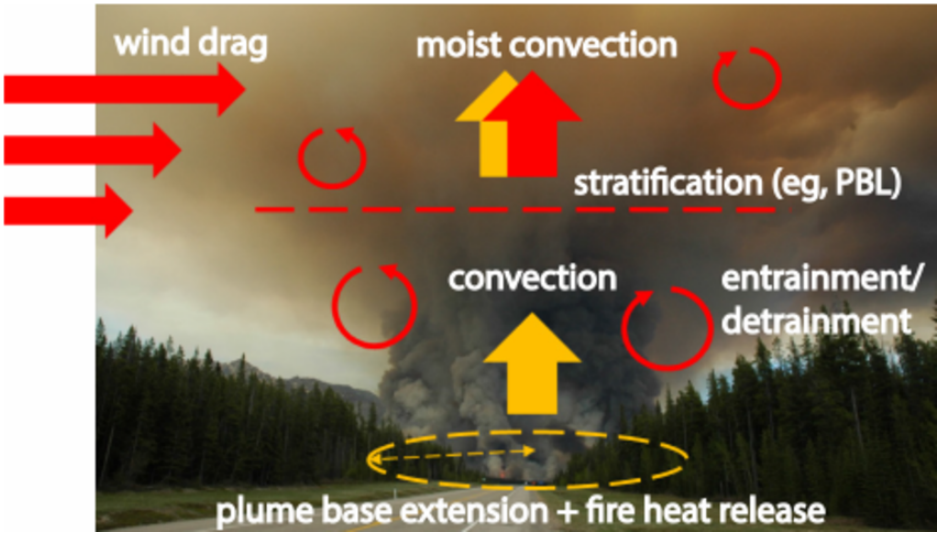

Figure 2.2: Conceptual diagram of the main physical processes governing wildfire plume dynamics, illustrating buoyancy, turbulent entrainment, and interaction with ambient atmospheric stratification. Based on Freitas & Paugam et al. (2016) [Paugam et al., 2016].

2.2.3 Long-Range Transport and Downwind Impacts

The processes described in the previous sections are particularly relevant for understanding the atmospheric impacts of large wildfire events, where intense emissions interact with meteorological conditions to produce effects far beyond the fire region. Wildfire-generated aerosols are often released in large quantities over short time periods and can be lofted to higher altitudes by fire-induced convection and strong synoptic-scale forcing. Once injected into the free troposphere, these particles can be transported hundreds to thousands of kilometers, influencing radiation, clouds, and air quality in downwind regions.

An additional mechanism contributing to vertical transport is **self-lofting**. Absorbing aerosols such as black carbon heat the surrounding air through aerosol–radiation interactions, creating positive buoyancy that can lift the smoke layer to higher altitudes even after it has left the fire region [Ohneiser et al., 2023]. This process has been observed to transport smoke from the troposphere into the stratosphere, where it can persist for months and spread globally.

Long-range transport of wildfire smoke is strongly controlled by large-scale atmospheric circulation patterns. Synoptic systems such as cyclones, frontal passages, and tropical-extratropical interactions can efficiently redistribute aerosols both horizontally and vertically. Under such conditions, wildfire plumes may interact with other aerosol types, such as mineral dust [Wyche et al., 2022], further modifying their optical and microphysical properties. The resulting aerosol layers can persist for several days and affect regions far removed from the original emission sources.

From a modeling perspective, capturing these processes requires a consistent representation of aerosol emissions, vertical redistribution, and transport within a dynamically evolving atmosphere. Similarly, observational analysis benefits from satellite-based products that provide information on aerosol loading and spatial extent, such as aerosol optical depth, as well as vertical information where available. The combination of satellite observations and online-coupled atmospheric modeling therefore provides a suitable framework for investigating the long-range impacts of extreme wildfire events.

3 October 2017 Iberian Wildfires

3.1 The Event

The October 2017 wildfires in the Iberian Peninsula constitute one of the most extreme wildfires episodes observed in southern Europe in recent decades.The fire began around 13 October in Galicia, northwestern Spain, and rapidly escalated over the following days [Chas-Amil et al., 2020]. By 15 October, fire activity peaked as Hurricane Ophelia passed off the Iberian coast, fanning the flames with exceptionally strong winds. In Portugal alone, firefighters battled over 440 fires on the worst day [Augusto et al., 2020]. The fires continued to burn until 18 October, when cooler temperature and rainfall finally assisted firefighting efforts [Ramos et al., 2023].

In total, more than 200,000 ha burned within a very short period, while an additional 42,000 ha were affected in Galicia (Fig. 3.1) [Ramos et al., 2023, Chas-Amil et al., 2020]. Characterized by rapid fire spread, widespread ignitions, and exceptionally high fire intensity, the event produced severe atmospheric emissions and large scale smoke transport. Between 13 and 18 October 2017, more than 7,900 wildfires affected northwestern Iberia, with 33 fires of significant size spreading rapidly due to drought and exceptional meteorological conditions [Mansilha et al., 2020].

The 2017 fire season in Portugal was record breaking in multiple respects. The total burned area of approximately 540,000 ha marked the highest value since reliable measurements began in 1980, representing nearly 60% of the total burned area in Europe that year [Ramos et al., 2023]. Tragically, 114 fatalities occurred during the season, with 50 deaths attributed directly to the October event. The economic losses exceeded USD 1.2 billion, and the local insurance sector declared it the costliest natural disaster in the country's history. Table 3.1 provides an overview of the key environmental, health, and economic impacts of the October 2017 wildfires.

Table 3.1: Summary of environmental, health, and economic impacts of the October 2017 Iberian wildfires.

Category	Indicator	Estimate
Environment	Burned area (Portugal)	> 200,000 ha
Air quality	Max PM_{10}	704 $\mu g\, m^{-3}$
Health	Excess mortality	50–114 deaths

Recent studies describe the episode as a compound event resulting from the concurrence of prolonged drought conditions, anomalously high temperature, strong wind associated with

Hurricane Ophelia, and human related ignition sources factors that simultaneously enabled extensive biomass burning and hampered suppression efforts [Ramos et al., 2023]. This chapter analyses these drivers in detail, drawing on meteorological reports and scientific literature to provide a comprehensive overview of the event.

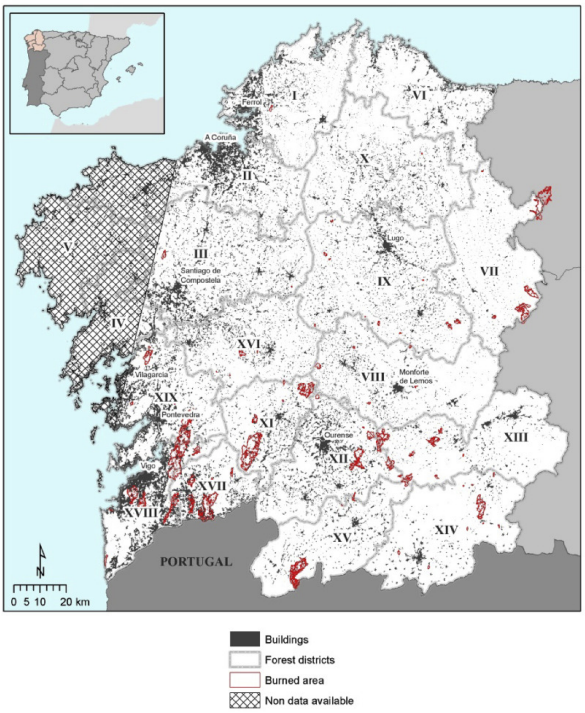

Figure 3.1: Burned area distribution in Galicia (northwestern Spain) during the October 2017 wildfires. Burned area perimeters derived from Sentinel-2 MSI imagery (12 and 27 October 2017). Adapted from Chas-Amil et al. [2020].

3.2 The Fire Triangle Framework

The compound nature of the 15 October 2017 event can be understood through the classical "fire triangle" concept, which identifies three necessary elements for wildfire: fuel, oxygen, and heat [Ramos et al., 2023]. The interaction of these three factors determines whether a fire can ignite and spread. In the following sections, each side of the triangle is examined in the context of the October 2017 Iberian wildfires.

- **Fuel:** The prolonged 2016/2017 drought preconditioned vegetation, creating abundant, dry, and highly flammable biomass across Portugal (Section 3.3).
- **Oxygen:** The passage of Hurricane Ophelia off the coast generated extreme southerly winds and critically low humidity, providing abundant oxygen and drying fuels further (Section 3.4)

- **Heat:** Over 500 human-related ignitions provided the initial heat sources (Section 3.5). The forecast of rain for the following day likely contributed to the high number of agricultural burns [Ramos et al., 2023].

Only when all three sides of the triangle converged did the unprecedented fire disaster occur. This framework highlights why the event cannot be attributed to a single cause; it was the compound interaction of drought, hurricane-force winds, and human activity that produced the exceptional outcome. Figure 3.2 summarises this interplay schematically.

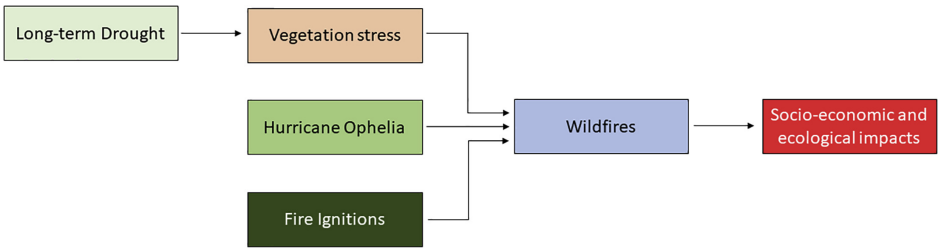

Figure 3.2: Schematic summary of the compound event drivers leading to the October 2017 wildfires. The diagram illustrates the interaction between the prolonged drought (fuel), the extreme winds and dry air from Hurricane Ophelia (oxygen), and the high number of human-related ignitions (heat). Adapted from Ramos et al. [2023].

3.3 Fuel: The 2016/2017 Drought

The exceptional fire weather on 15 October acted upon vegetation already under severe hydric stress due to a prolonged drought. The 2016/2017 drought was unprecedented in western and central Europe, affecting more than 90% of the region and reaching record-breaking values in 25% of the area [Ramos et al., 2023]. The drought was driven by consecutive blocking anticyclones and subtropical ridges displaced from their typical locations, leading to persistent positive geopotential height anomalies.

In Portugal, dry conditions began in July 2016 and lasted until May 2018, classifying the event as a hydrological drought persisting for nearly two years [Ramos et al., 2023]. September 2017 had been the driest month in 87 years, with approximately 81% of Portuguese territory under severe drought and 7.4% in extreme drought [Mansilha et al., 2020]. The accumulated 1-month SPEI (Standardized Precipitation-Evapotranspiration Index) for Portugal fell below the 10th percentile, marking the event as the most severe European drought at the continental scale since at least 1979.

The impact on vegetation is evident from Normalized Difference Vegetation Index (NDVI) anomalies. NDVI is a satellite-derived index that measures vegetation health by comparing the reflectance of near-infrared light (strongly reflected by healthy vegetation) and red light (absorbed by chlorophyll) [Huang et al., 2021, Joiner et al., 2018]. The index is calculated as:

$$\mathrm{NDVI} = \frac{\rho_{\mathrm{NIR}} - \rho_{\mathrm{Red}}}{\rho_{\mathrm{NIR}} + \rho_{\mathrm{Red}}}$$

where ρ_{NIR} is the reflectance in the near-infrared spectral band and ρ_{Red} is the reflectance in the red spectral band [Huang et al., 2021]. Values range from -1 to 1, with higher values indicating denser, healthier vegetation. Low or negative NDVI values indicate sparse vegetation, stressed plants, or barren surfaces such as rock, sand, or snow [Huang et al., 2021].

By October 2017, negative NDVI anomalies were widespread across Portugal (Fig. 3.3), indicating severely stressed and flammable vegetation. This preconditioning was essential for the rapid fire spread observed on 15 October.

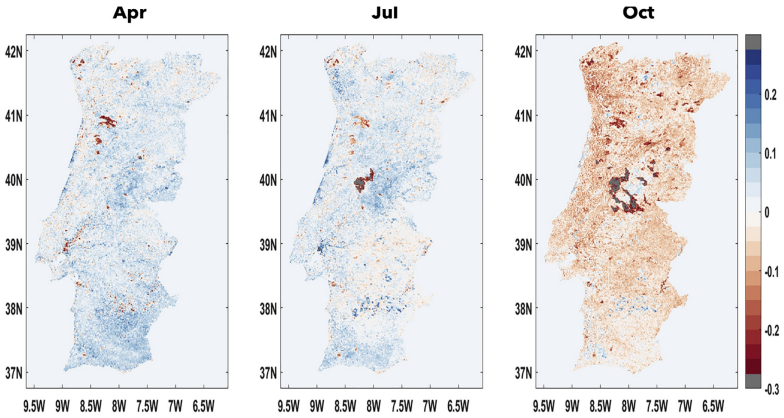

Figure 3.3: NDVI anomalies for April, July, and October 2017. Gray pixels indicate cloud-contaminated areas not considered in the analysis. Widespread negative anomalies in October reflect severe vegetation stress following the prolonged drought. Adapted from Ramos et al. [2023].

3.4 Oxygen: Hurricane Ophelia

3.4.1 Meteorological Evolution

Ophelia originated in the central subtropical Atlantic in early October 2017 and was named by the U.S. National Hurricane Center as a tropical depression on 9 October [Moore, 2018]. Over the following days, it strengthened steadily, becoming a Category 1 hurricane on 11 October and reaching its peak intensity as a Category 3 major hurricane on 14 October – the farthest east such system ever recorded in the Atlantic basin.

By 15 October, Ophelia had begun to weaken as it became embedded within the fast flow of a large mid-latitude trough moving eastwards across the Atlantic. Crucially for the Iberian fires, Ophelia remained positioned off the coast of Portugal on this day, steering an intense southerly flow over the continent due to the strong pressure gradient associated with the

hurricane. Extratropical transition was completed early on 16 October, after which the post-tropical cyclone traveled northward and made landfall in Ireland later that day [Moore, 2018].

3.4.2 Role in the Iberian Fires

A very strong southerly flow was steered over continental Portugal due to the intense pressure gradient associated with the hurricane [Ramos et al., 2023]. This circulation advected a warm and dry air mass originating from northern Africa.

On 15 October, sustained southerly winds of 30-40 km/h were recorded in central Portugal, with gusts reaching 50-80 km/h during the afternoon - exceptionally strong values for October [Ramos et al., 2023]. Near-surface relative humidity dropped below 20% across widespread areas, and 70% of weather stations recorded temperatures above 30°C, breaking October records at many coastal stations north of Lisbon.

These conditions represent extreme fire weather, the combination of high temperatures, low humidity, strong winds, and absence of rainfall that promotes fire ignition and rapid spread [Goodrick et al., 2017]. Importantly, Ophelia remained sufficiently far offshore that the moist tropical air associated with its core and outer bands did not reach the continent. This meant that no rainfall relief accompanied the extreme fire weather. The following day, as Ophelia moved towards Ireland, cold and humid air intruded over western Iberia, bringing rainfall that assisted in extinguishing the remaining fires [Ramos et al., 2023].

3.5 Heat: Human-Related Ignitions

Meteorological conditions alone do not cause wildfires; an ignition source is required. On 15 October 2017, more than 500 ignitions were recorded in Portugal - an extraordinarily high number. Most of these ignitions were of human origin and related to agricultural practices. The forecast of rain for the following day likely contributed to the high number of agricultural burns, as farmers may have conducted burning under the expectation that rainfall would extinguish the fires [Ramos et al., 2023]. Instead, the extreme fire weather caused these ignitions to develop into major, uncontrollable wildfires.

3.6 Biomass Burning Emissions and Air Quality Impacts

The fires generated exceptionally large emissions of particulate matter and trace gases from biomass combustion. Observed daily PM_{10} concentrations in affected regions reached values up to $704\,\mu g\,m^{-3}$, far exceeding European air quality standards and typical background levels [Augusto et al., 2020, Oliveira et al., 2020]. Emissions estimates indicate that particulate matter and carbon monoxide released during the October 2017 fires exceeded total

Portuguese anthropogenic emission for the entire year 2017, underlining the magnitude of the biomass burning source [Fernandes et al., 2022].

3.7 Downwind Effects: The "Red Sky" Phenomenon

The intensity of the fires generated substantial smoke emissions that were efficiently transported across western Europe by the same synoptic system. Strong southerly winds ahead of Storm Ophelia advected smoke plumes northward and eastward, impacting Spain, France, Belgium, the Netherlands, and the United Kingdom [Augusto et al., 2020]. Downwind populations were exposed to additional PM_{10} concentrations of approximately $10\,\mu g\,m^{-3}$ to $12\,\mu g\,m^{-3}$ over several days [Augusto et al., 2020].

A striking example of such long-range transport is shown in Figure 3.4. The satellite image illustrates the spatial extent of the transported aerosol plume on 17 October 2017, demonstrating how smoke from the Iberian Peninsula reached central Europe, including Germany, within a few days under favorable synoptic conditions.

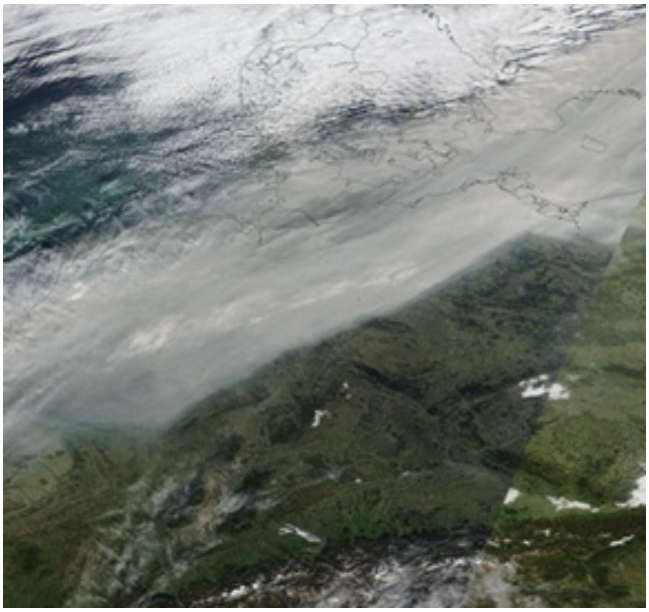

Figure 3.4: Satellite image from 17 October 2017 showing an extensive aerosol plume over central Europe originating from the Iberian Peninsula wildfires. The image illustrates the long-range transport of wildfire smoke toward Germany. Source: NASA Worldview (MODIS imagery).

The same circulation also transported Saharan dust, which mixed with wildfire smoke and further enhanced particulate loadings across downwind regions. The unique "red sky" phenomenon observed over the United Kingdom on 16 October 2017 resulted from this complex aerosol mixture [Wyche et al., 2022].

Figure 3.5 shows a true color RGB image, revealing the extensive cloud top associated with Storm Ophelia. Red dots over the Iberian Peninsula indicate heat anomalies from active fires,

visually confirming the source region of biomass burning aerosols that were subsequently transported northward within the storm's circulation.

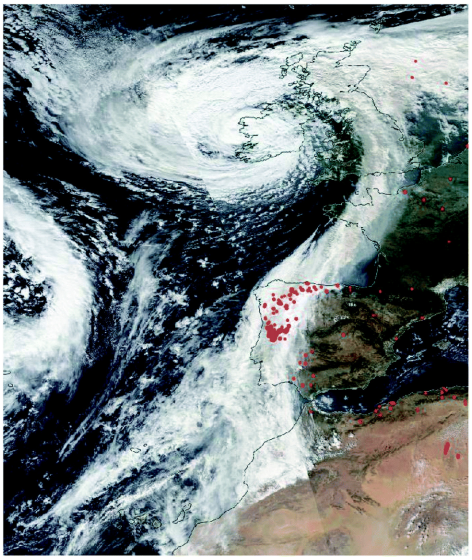

Figure 3.5: True color RGB corrected reflectance visualization of the cloud top on 16 October 2017, derived from Suomi NPP VIIRS data. Areas of high-density heat anomalies, indicating fires, are highlighted as red dots (NASA Worldview). Adapted from Wyche et al. [2022].

Back-trajectory analysis using the HYSPLIT model confirms that air masses arriving over the UK on 16 October had previously traversed the Iberian Peninsula and North Africa, supporting this mixed aerosol source attribution [Wyche et al., 2022].

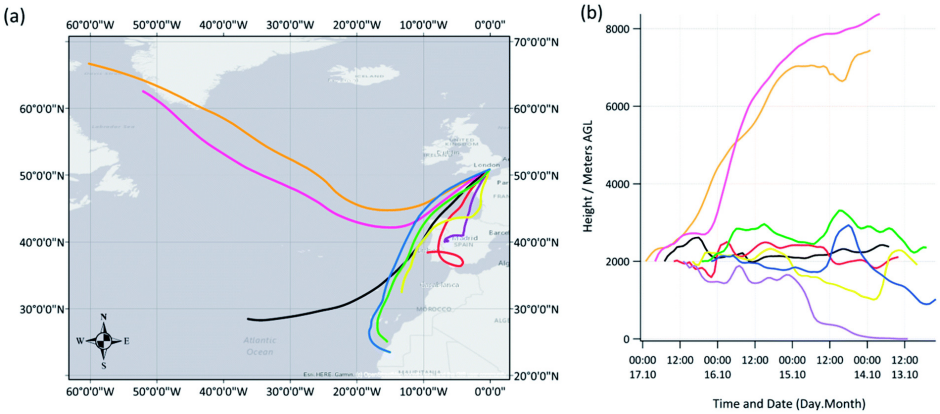

Figure 3.6: 72-hour HYSPLIT back-trajectory analysis for air masses arriving over the UK on 16 October 2017 at 2000 m altitude, showing origins over Iberia and North Africa. Adapted from Wyche et al. [2022].

This coupling between intense biomass burning and large scale atmospheric circulation makes the October 2017 Iberian wildfires a particularly suitable case for studying aerosol emissions, vertical redistribution, and long-range transport processes.

4 Data and Methods

4.1 Model Description

Numerical weather prediction (NWP) models provide a physically consistent framework for simulating the temporal evolution of the atmosphere by solving a system of equations derived from fundamental and conservation laws, including the conservation of mass, momentum, and energy. Although these laws are common to all atmospheric models, individual models differ in their mathematical formulation and numerical solution methods. NWP models describe the temporal development of key atmospheric variables such as temperature, pressure, wind, water vapor, clouds, and precipitation. Many relevant processes, including cloud formation and radiative interactions, occur on spatial scales smaller than the model grid and are, therefore, represented through parametrization schemes that account for subgrid scale processes [Deutscher Wetterdienst].

For the investigation of wildfire events, it is necessary to use a modeling framework that consistently represents both meteorological processes and aerosol dynamics. Wildfires emit large amounts of aerosol particles and trace gases that are transported over long distances and can interact with radiation and clouds. In this thesis, the ICON-ART model system is used to simulate the October 2017 wildfire event over the Iberian Peninsula, as it combines a non-hydrostatic atmospheric model with an explicit treatment of aerosols and reactive trace gasses.

4.1.1 The ICON Modeling Framework

The ICOsahedral NonHydrostatic ICON model is a numerical weather prediction and climate modeling system developed jointly by German Weather Service (Deutscher Wetterdienst) (DWD) and the Max Planck Institute for Meteorology (MPI-M)[Zängl et al., 2015]. The ICON partnership has since expanded to include the German Climate Computing Center DKRZ and the Karlsruhe Institute of Technology (KIT) and Center for Climate Systems Modeling (C2SM) included as a development partner. ICON became operational at DWD for numerical weather prediction in January 2015 and is designed as a unified modeling framework that can be applied across spatial scales, ranging from global simulations to limited-area and nested regional domains [Zängl et al., 2015, Giorgetta et al., 2018].

Numerical weather prediction models represent the continuous atmosphere on a discrete spatial grid to enable numerical integration. The ICON model employs a horizontally

unstructured triangular mesh covering the spherical Earth's surface, avoiding the meridian convergence present in conventional latitude-longitude grids and following uniform resolution across the globe.

The ICON horizontal grid is constructed from a spherical icosahedron consisting of 20 triangular faces. Through hierarchical refinement of this base geometry, a sequence of global icosahedral-triangular Arakawa C grids is generated, enabling increasingly fine spatial resolution while preserving near uniform cell areas. This approach reduces numerical distortions associated with polar regions and forms the basis of ICON's global discretization strategy [2012].

Horizontal grid resolution in ICON is commonly described using the RnBk notation, where n denotes the number of initial subdivisions of each icosahedron edge and k indicates the number of subsequent bisection steps. For a given grid configuration, the total number of horizontal grid cells depends on these refinement parameters and determines the effective horizontal resolution of the model. The number of horizontal cells is given by:

$$n_{\text{cell}} = 20\, n^2\, 4^k \tag{4.1}$$

An estimate of the effective horizontal grid spacing, Δx, can be derived from the total number of grid cells and the Earth's mean radius r_{e}:

$$\Delta x = \sqrt{\frac{4\pi}{n_{\text{cell}}}}\, r_{\text{e}} \tag{4.2}$$

In the vertical dimension, ICON employs a generalized terrain-following coordinate system that transitions from orography following levels near the surface to surfaces of constant geometric height in the upper atmosphere [Leuenberger et al., 2010]. This hybrid approach is essential for the non-hydrostatic formulation of ICON, as it maintains numerical stability in the upper atmosphere while accurately representing boundary layer processes near the surface [Weimer et al., 2017]. The design mitigates the numerical inaccuracies that can arise from strong grid deformation over steep topography, which is a known limitation of conventional terrain following coordinates.

ICON uses a fully compressible, non hydrostatic dynamical core and therefore does not rely on the hydrostatic approximation. This formulation enables consistent application across global and regional scales, including fine resolution at which hydrostatic approximation is no longer valid. The NWP physics components, as detailed by Zängl et al. [2015], consists of parametrization for radiative transfer, cloud microphysics, convection, turbulent diffusion, and surface interactions, which are specifically optimized for numerical weather prediction applications.

The model solves a set of prognostic equations for momentum, thermodynamic variables, density, and trace gases and aerosols. These equations are formulated in flux form to ensure exact local mass conservation and mass consistent transport. The governing equation

systems follows the choice of prognostic variables proposed by Gassmann and Herzog [2008] and consists of:

- the momentum equations (horizontal and vertical) 4.3, 4.4,
- the thermodynamic energy equation (first law of thermodynamics) 4.5,
- the continuity equation (mass conservation) 4.6, and
- tracer conservation equations for atmospheric constituents 4.7.

$$\frac{\partial \hat{v}_n}{\partial t} + \frac{\partial \hat{K}_h}{\partial n} + (\hat{\zeta} + f)\,\hat{v}_t + \hat{w}\,\frac{\partial \hat{v}_n}{\partial z} = -c_{pd}\,\hat{\theta}_v\,\frac{\partial \hat{\pi}}{\partial n} - \frac{1}{\bar{\rho}}\left(\nabla_h \cdot \overline{\rho\,\mathbf{v}''\mathbf{v}''}\right)\cdot \mathbf{e}_n \tag{4.3}$$

$$\frac{\partial \hat{w}}{\partial t} + \hat{\mathbf{v}}_h \cdot \nabla \hat{w} + \hat{w}\,\frac{\partial \hat{w}}{\partial z} = -c_{pd}\,\hat{\theta}_v\,\frac{\partial \hat{\pi}}{\partial z} - g - \frac{1}{\bar{\rho}}\,\frac{\partial}{\partial z}\left(\overline{\rho\,w''v''}\right) \tag{4.4}$$

$$\frac{c_{vd}c_{pd}}{R_d}\,\bar{\rho}\,\hat{\theta}_v\,\frac{\partial \hat{\pi}}{\partial t} + c_{pd}\,\bar{\pi}\,\nabla\cdot\left(\bar{\rho}\,\hat{\mathbf{v}}\,\hat{\theta}_v\right) = c_{pd}\,\bar{\pi}\,\bar{\rho}\,\hat{\theta}_v\,\nabla\cdot\hat{\mathbf{v}} + c_{pd}\,\bar{\pi}\,\bar{\rho}\,\bar{Q} \tag{4.5}$$

$$\frac{\partial \bar{\rho}}{\partial t} + \nabla\cdot(\bar{\rho}\,\hat{\mathbf{v}}) = 0 \tag{4.6}$$

$$\frac{\partial \bar{\rho}\,\hat{q}_k}{\partial t} + \nabla\cdot(\bar{\rho}\,\hat{q}_k\,\hat{\mathbf{v}}) = -\nabla\cdot\left(\overline{\mathrm{J}_k^z} + \overline{\rho\,q_k''\mathbf{v}''}\right) + \bar{\sigma}_k \tag{4.7}$$

Equation 4.3 describes the evolution of the horizontal wind component normal to the triangle edges, while equation 4.4 governs the vertical wind component. The thermodynamic energy equation (Equation 4.5) represents the first law of thermodynamics. Equation 4.6 is the continuity equation, ensuring mass conservation. Finally Equation 4.7 governs the conservation of trace species such as aerosols and reactive gases.

In order to separate turbulent fluctuations from the resolved mean flow, ICON applies a density-weighted averaging, commonly referred to as Hesselberg averaging [Turner, 1927]. Any prognostic variable ϕ is decomposed into a density-weighted mean component and a corresponding deviation,

$$\phi = \hat{\phi} + \phi'', \tag{4.8}$$

where the deviation from the mean is denoted by ϕ, and the density-weighted (barycentric) mean is defined as

$$\hat{\phi} = \frac{\overline{\rho\phi}}{\overline{\rho}}, \tag{4.9}$$

with $\overline{\rho}$ representing the mean air density an $\overline{phi}$ denoting the standard Reynolds average. This averaging approach is particularly suitable for compressible flow and ensures a consistent treatment of mass, momentum, and thermodynamic variables. A detailed discussion of density-weighted averaging calculus can be found in Zdunkowski and Bott [2003].

Within this framework, the prognostic variables in ICON are :

- the horizontal wind velocity component normal to the triangle edges, $\hat{v}_n$,

- the tangential horizontal wind components to the triangle edges, $\hat{v}_t$ (which together with $\hat{v}_n$ and vertical velocity forms a right-handed coordinate system),
- the vertical wind component, $\hat{w}$
- the air density, $\bar{\rho}$
- and the virtual potential temperature $\hat{\theta}_v$.

Additional dynamic quantities include the vertical vorticity $\hat{\zeta}$, the Coriolis parameter f, and the horizontal kinetic energy

$$\hat{K}_h = \frac{1}{2}\left(\hat{v}_n^2 + \hat{v}_t^2\right). \tag{4.10}$$

Thermodynamic relationships are expressed using the Exner pressure function,

$$\pi = \left(\frac{R_d}{p_{00}}\rho\theta_v\right)^{\frac{R_d}{c_{vd}}}, \tag{4.11}$$

where R_d is the gas constant of dry air, c_{pd} and c_{vd} are the specific heat capacities at constant pressure and volume, respectively, and $p_{00} = 1000$ hPa is the reference pressure. Turbulent momentum fluxes and diabatic heating are represented through appropriate source terms in the governing equations, while horizontal derivatives are evaluated in the edge-normal direction of the triangular grid.

4.1.2 The ICON-ART Model Extension

The Aerosols and Reactive Trace gases (ART) extension enhances the ICON model by enabling explicit simulation of aerosol and trace gas transport within the atmospheric flow. Developed and maintained at the Karlsruhe Institute of Technology (KIT) in cooperation with the German Weather Service (DWD) [Rieger et al., 2015, Schröter et al., 2018], ART is fully integrated into ICON through dedicated interface modules.

The ART extension represents the emission, transport, transformation, and removal of aerosols and gaseous species in a dynamically consistent manner. By coupling composition processes directly to the meteorological core, ICON-ART accounts for interactions between aerosols, trace gases, radiation, clouds, and atmospheric dynamics without requiring offline chemical transport modeling [Schröter et al., 2018]. Figure 4.1 in Hoshyaripour et al. [2026] illustrate this coupling between meteorological and aerosol components.

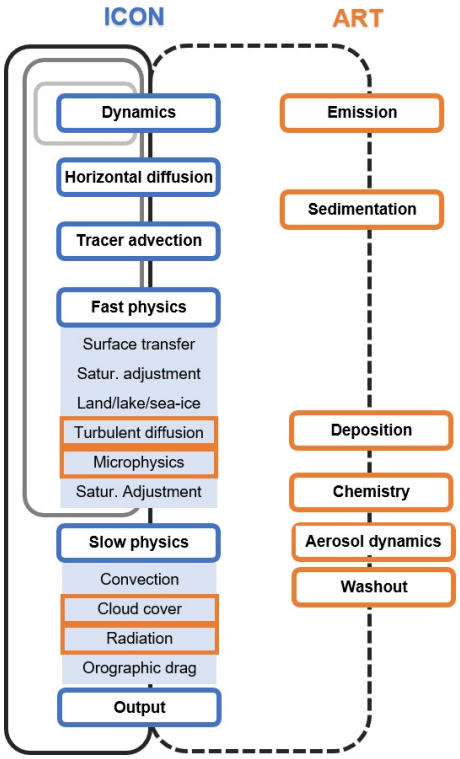

Figure 4.1: Schematic overview of the coupling between ICON and the ART extension. Blue boxes indicate processes within the ICON dynamical core and physics packages, while orange boxes represent processes implemented in ART. Orange frames around selected ICON processes denote that ART tracers are handled within the ICON tracer framework. The gray and black contours illustrate the sequence of time integration steps. Adapted from Hoshyaripour et al. [2026].

A key feature of ART is its flexible tracer framework, which allows experiment specific tracer sets depending on the spatial scale and scientific focus. The tracer framework is compatible with different ICON physics configurations, ensuring that changes in physical parameterizations do not require modifications of the ART code itself [Schröter et al., 2018].

4.1.2.1 Basic Equations

Following Rieger et al. [2015], the treatment of gases and aerosols in ICON-ART employs the same density-weighted (barycentric) averaging approach as used in the ICON dynamical core (Section 4.1.1). This formulation also forms the basis for the prognostic aerosol equations described in Hoshyaripour et al. [2026].

In this framework, the fluctuation from the density-weighted mean is defined as

$$\Psi'' = \Psi - \hat{\Psi}. \tag{4.12}$$

where the overbar denotes Reynolds averaging and ρ is the air density.

The total time derivative in this framework is expressed as

$$\frac{\hat{d}}{dt} = \frac{\partial}{\partial t} + \hat{\mathbf{v}} \cdot \nabla, \tag{4.13}$$

with $\hat{\mathbf{v}}$ representing the barycentric mean velocity. The continuity equation 4.6 then takes the form

$$\frac{\hat{d\overline{\rho}}}{dt} = -\overline{\rho}\, \nabla \cdot \hat{\mathbf{v}}. \tag{4.14}$$

In ICON-ART, the evolution of aerosols is described by prognostic equations for both the number concentration (zeroth moment) and mass mixing ratio (third moment) of each aerosol mode. These equations extend the tracer continuity by equation by including additional process terms representing advection, turbulent transport, sedimentation, emissions, and removal processes. Each physical process appears as a distinct term in the governing equations, enabling a process based interpretation of aerosol evolution [Hoshyaripour et al., 2026, Muser et al., 2020].

For a generic aerosol mode l, the prognostic equations for the specific number concentration $\hat{\Psi}_{0,l}$ and mass mixing ratio $\hat{\Psi}_{3,l}$ are Hoshyaripour et al. [2026]:

$$\frac{\partial(\overline{\rho}\hat{\Psi}_{0,l})}{\partial t} = -\nabla \cdot (\hat{\mathbf{v}}\, \overline{\rho}\hat{\Psi}_{0,l}) - \nabla \cdot (\overline{\rho v'' \Psi''_{0,l}}) + \frac{\partial}{\partial z}\left(v_{\text{sed},0,l}\, \overline{\rho}\hat{\Psi}_{0,l}\right) - W_{0,l} + E_{0,l}, \tag{4.15}$$

$$\frac{\partial(\overline{\rho}\hat{\Psi}_{3,l})}{\partial t} = -\nabla \cdot (\hat{\mathbf{v}}\, \overline{\rho}\hat{\Psi}_{3,l}) - \nabla \cdot (\overline{\rho v'' \Psi''_{3,l}}) + \frac{\partial}{\partial z}\left(v_{\text{sed},3,l}\, \overline{\rho}\hat{\Psi}_{3,l}\right) - W_{3,l} + E_{3,l}, \tag{4.16}$$

where:

- $\hat{\mathbf{v}}$ is the barycentric mean velocity,
- $\nabla \cdot (\overline{\rho v'' \Psi''_l})$ represents turbulent mixing,
- $v_{\text{sed},0,l}$ and $v_{\text{sed},3,l}$ are the sedimentation velocities for number and mass, respectively,
- $W_{0,l}$ and $W_{3,l}$ are the loss rates due to wet deposition (washout),
- $E_{0,l}$ and $E_{3,l}$ are the emission fluxes for number and mass from the fire source.

4.1.2.2 Representation of aerosol dynamics

Aerosols in ICON-ART are represented using a model approach within the AERODYN (AEROsol DYNamics) framework [Muser et al., 2020, Hoshyaripour et al., 2026], in which particle populations are described by log-normal size distributions [Rieger et al., 2015]. This approach provides a computationally efficient representation of the aerosol size spectrum by characterizing each mode through a limited set of parameters.

The particle size distribution in each mode is given by a lognormal function [Zender, 2008]:

$$n(D) = \frac{N}{\sqrt{2\pi}\,\ln\sigma_g}\frac{1}{D}\exp\left[-\frac{(\ln D - \ln D_g)^2}{2(\ln\sigma_g)^2}\right], \tag{4.17}$$

where N is the total number concentration, D_g is the geometric mean diameter, and σ_g is the geometric standard deviation.

In the present configuration, soot is represented in four transported modes:

- Insoluble Aitken mode (insol_ait): $D_{g,n} = 20$ nm, $\sigma_g = 1.7$
- Mixed Aitken mode (mixed_ait): $D_{g,n} = 20$ nm, $\sigma_g = 1.7$
- Insoluble accumulation mode (insol_acc): $D_{g,n} = 150$ nm, $\sigma_g = 2.0$
- Mixed accumulation mode (mixed_acc): $D_{g,n} = 150$ nm, $\sigma_g = 2.0$

The mixed modes represent soot internally mixed with soluble aerosol components (sulfate, ammonium, nitrate, and aerosol water). Soot emissions are prescribed using a single lognormal emission mode with $\sigma_g = 2.0$ and characteristic diameters 70 nm for number and 269 nm for mass. The emitted mass is distributed among the transported modes according to the size distribution.

In this study, aerosol microphysical processes such as nucleation, condensation, coagulation, and mode shifting (aging) are not activated. Therefore, the evolution of soot aerosols is governed solely by the processes represented in Eqs. 4.15 and 4.16:

- **Advection**: Transport by the resolved wind field.
- **Turbulent diffusion**: Vertical mixing due to sub-grid turbulence, parameterized with a one-dimensional prognostic turbulent kinetic energy scheme.
- **Sedimentation**: Gravitational settling, treated as an additional vertical advection with downward velocity.
- **Wet deposition**: Aerosol washout (iart_aero_washout = 1).
- **Dry deposition**: Removal at the surface via a resistance approach.
- **Emissions**: Fire emissions from GFAS (iart_fire = 1) distributed vertically by the plume-rise model (Section 4.2.2).

Figure 4.2 illustrates the modal framework and the various processes; in this study, only the modal representation is used, and the depicted microphysical processes are switched off.

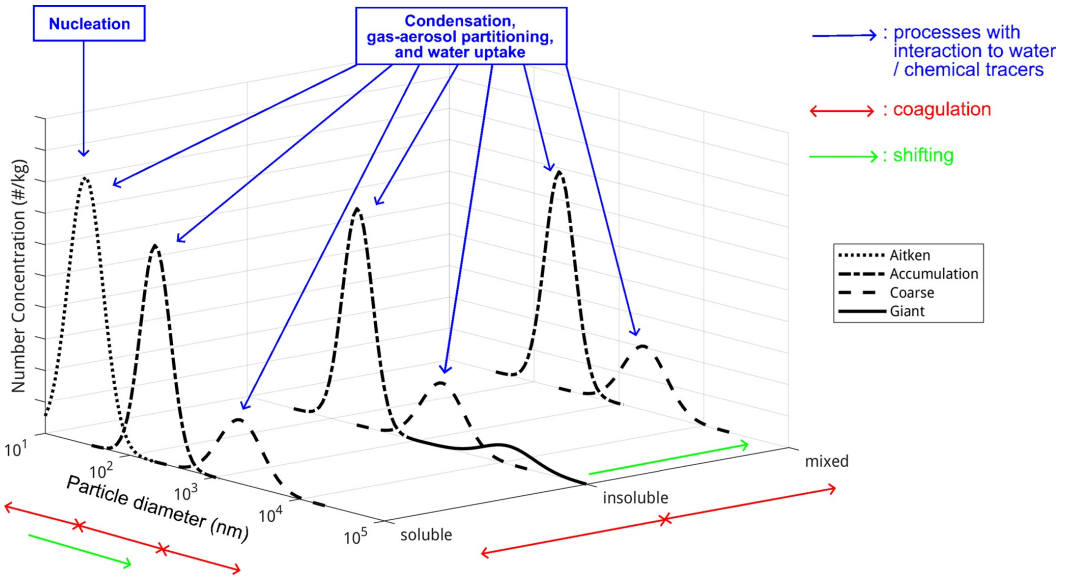

Figure 4.2: Schematic representation of the modal aerosol framework in ICON-ART. Aerosols are represented by lognormal size distributions corresponding to Aitken, accumulation, coarse, and giant modes. The diagram illustrates key aerosol dynamical processes including nucleation, condensation, coagulation, and mode shifting between soluble, insoluble, and mixed states. Adapted from Hoshyaripour et al. [2026].

4.1.3 Aerosol-radiation interaction

In ICON-ART, aerosol-radiation interactions are represented through the ecRad radiation scheme [Hogan and Bozzo, 2018, Rieger et al., 2015]. For each aerosol type, the model calculates the three key optical properties described in Section 1.1: the mass extinction coefficient, single scattering albedo, and asymmetry parameter. These properties are passed to the radiation scheme, which computes heating rates that feed back into the model's dynamics. ART provides two approaches for obtaining aerosol optical properties: precomputed lookup tables that account for size distribution variability, or online calculation using MieAI for more flexible representation of particle composition and mixing state [Hoshyaripour et al., 2026]. The module also includes forward operators to diagnose aerosol optical depth (AOD) for comparison with observations [Hoshyaripour et al., 2026]. This coupling between aerosol fields and the radiative transfer calculations allows ICON-ART to simulate the two-way interactions between aerosols and radiation over the course of a simulation.

4.2 Treatment of biomass burning in ICON-ART

Accurate representation of biomass-burning emissions in atmospheric models requires knowledge of fire location, temporal evolution, and emission strength. In ICON-ART, these quantities are obtained from the Global Fire Assimilation System (GFAS), introduced in the following section.

4.2.1 The Global Fire Assimilation System (GFAS)

The Global Fire Assimilation System (GFAS) was developed as part of the Monitoring Atmospheric Composition and Change (MACC) project, funded by the European Union to provide global atmospheric composition monitoring and forecasting services [Kaiser et al., 2012]. GFAS provides estimates of emissions originating from biomass burning based on Fire Radiative Power (FRP) observations. FRP quantifies the thermal radiation released by fires in units of Watts for each satellite pixel and is measured by the Moderate Resolution Imaging Spectroradiometer MODIS onboard the polar-orbiting satellites Aqua and Terra.

GFAS provides daily estimates of gases and aerosols released by biomass burning worldwide on a global grid with 0.1° resolution, and has been widely used in atmospheric composition modeling [Kaiser et al., 2012].

Raw satellite data contains gaps due to cloud cover and false signals from volcanoes or industrial sources. GFAS addresses these issues by filtering outspurious observations and filling gaps using a Kalman filter, which combines previous and current FRP measurements to estimate fire activity in cloud-covered areas [Kaiser et al., 2012]. A land fraction mask also corrects for errors introduces by water bodies.

The FRP is then converted to emissions in two steps. First, the combustion rate (biomass burned per area) is calculated using land cover specific conversion factors. Second, emission factors for different chemical species (e.g., carbon monoxide, black carbon, organic matter) determine how much of each species is released per kilogram of burned biomass [Kaiser et al., 2012, Hoshyaripour et al., 2026].

A known limitation is that GFAS underestimates organic matter and black carbon emissions when compared to global observations. To correct this, Kaiser et al. [2012] recommend applying an enhancement factor of 3.4 to these aerosol species based on comparisons with aerosol optical depth observations. This factor is applied in the simulations presented in this thesis to ensure realistic smoke concentrations.

4.2.2 The plume rise model

Wildfire emissions are often injected well above the surface due to the intense heat released by fires. Atmospheric models with horizontal resolutions on the order of 10-100 km cannot explicitly resolve the convective processes that govern this vertical transport. To account for this sub-grid scale phenomenon, ICON-ART incorporates a one-dimensional plume rise parametrization based on Freitas et al. [2006, 2007], implemented analogously to its implementation in COSMO-ART [Walter et al., 2016]. This 1-D model has a vertical grid spacing of 100 m (200 vertical layers) and is integrated into the 3-D host model (ICON-ART).

The model estimates plume height from properties of the fire, such as heat flux, combined with information on the atmospheric surroundings, including stability and flow conditions. Fire location is combined with land-use data to categorize vegetation type (forest,

woody savanna, or grassland), each with associated heat flux ranges [Freitas et al., 2006]. Environmental conditions including temperature, pressure, humidity, and wind speed are provided by ICON for each active fire grid point. Based on these inputs, the plume rise model calculates the vertical velocity of the rising smoke parcel. The plume top is defined as the height where this vertical velocity drops below 1 m s^{-1}, indicating that buoyancy is no longer sufficient to overcome atmosphere stability [Walter et al., 2016, Hoshyaripour et al., 2026].

The outputs are the upper and lower bounds of the emissions are distributed following a prescribed parabolic vertical profile [Walter et al., 2016], ensuring that aerosols and trace gases are injected at altitudes consistent with the fire's intensity and prevailing atmospheric conditions. This approach is critical for simulating long-range transport, as aerosols injected into the free troposphere have longer lifetimes and can be transported over much greater distances than those remaining near the surface see Chapter 2, Section 2.2.3 for further discussion.

To represent the observed diurnal cycle of fire activity with peak emissions in the early afternoon and minima at night a Gaussian diurnal cycle function peaking around 13:00-14:00 local time is applied to fire intensity and emissions [Kaiser et al., 2012, Andela et al., 2015]. This temporal variability is important for accurately timing the injection of smoke into the atmosphere.

4.2.3 Additional sensible heat release

In the current version of ICON-ART, there is the option to take the sensible heat flux released during combustion into consideration, as described by Hoshyaripour et al. [2026]. To better capture fire-induced changes in atmospheric dynamics, this sensible heat release term is included following the implementation described by Muth et al. [2025]. The term was already implemented in the model version used for this thesis.

The parametrization uses the Fire Radiative Power (FRP) from GFAS. The sensible heat flux from the fire, sh_{fire}, is calculated as:

$$sh_{\text{fire}} = d(t) \cdot 0.55 \cdot 10 \cdot \text{FRP} \tag{4.18}$$

Where FRP is the Fire Radiative Power (W m^{-2}), the factor 10 converts radiative to total fire energy [Val Martin et al., 2012, Ke et al., 2021]. 0.55 represents the convective fraction of total energy [Freitas et al., 2006], and $d(t)$ is a diurnal cycle function accounting for peak fire intensity during early afternoon hours [Andela et al., 2015, Walter et al., 2016]. The resulting sensible heat flux is added to the existing surface heat flux already present in ICON.

To investigate the effect of a potential underestimation of FRP in GFAS (from which both the aerosol emissions and the heat release are derived), an enhancement factor was applied to the sensible heat release. Following Kaiser et al. [2012], a factor of SHR = 3.4 was

tested, as this value corrects the assumed underestimation of soot emissions. A second experiment was conducted with a doubled factor of SHR = 6.8 to examine sensitivity to a larger enhancement.

4.3 Simulation setup

ICON-ART simulations were performed to reproduce the wildfire smoke transport during October 2017. The model was run globally on an ICON R03B07 grid with horizontal resolution of approximately 13 km and 90 vertical levels. Meteorological initial conditions were provided by Integrated Forecasting System (IFS) and converted to ICON initial conditions using ifs2icon preprocessing workflow. The simulations start on 13 October 2017 at 00:00 UTC and cover a period of six days. Model output was written at hourly intervals.

Biomass burning emissions were taken from the Global Fire Assimilation System (GFAS) [Kaiser et al., 2012]. BC and organic carbon (OC) emissions were combined to represent soot emissions used in aerosol module. The emission fields were conservatively remapped to the ICON grid to preserve the total emitted mass. Fire radiative power (FRP) from GFAS was used to derive sensible heat release from the fires, which was added to the surface sensible heat flux and influences plume rise [Muth, 2024].

Regarding aerosol processes, only transport and aerosol-radiation interactions were activated in the simulations. Microphysical processes such as nucleation, condensation, and coagulation were disabled, as the focus of this study is on the transport and radiative effects of wildfire smoke rather than detailed aerosol microphysics.

To investigate the sensitivity of simulated aerosol fields to aerosol-radiation interactions, simulations were performed both with and without the activation of ARI. In all experiments, the soot emissions were scaled by a factor of 3.4 following Kaiser et al. [2012] to account for the known underestimation in GFAS. In addition, two different scalings of the sensible heat release were tested: SHR = 3.4 and SHR = 6.8, to examine the influence of fire-induced heating on plume rise and transport. All other model settings were kept identical between experiments.

Model output was interpolated from the native ICON-ART R03B07 grid (approximately 13 km horizontal resolution) to a regular $0.2^\circ \times 0.2^\circ$ latitude–longitude grid (remap = 1), and all analyses presented in this study were performed on this grid. Figure 4.3 shows the geographical focus of the analysis. Although the model was run globally, the analysis concentrates on the European domain, with the Iberian Peninsula marking the source region of wildfire emissions and Germany representing the downwind region affected by long-range transport of smoke aerosols.

Figure 4.3: Geographical overview of the analysis region. The Iberian Peninsula marks the source region of the October 2017 wildfire emissions, while Germany represents the downwind region affected by long-range transport of smoke aerosols. Red stars indicate the approximate locations of the emission and analysis regions.

4.4 Satellite Data

4.4.1 CALIPSO Attenuated Backscatter

The Cloud-Aerosol Lidar and Infrared Pathfinder Satellite Observation (CALIPSO) mission provides global vertical profiles of aerosols and clouds using an active lidar instrument [Ruiz de Morales et al., 2026]. The Level 1 total attenuated backscatter at 532 nm is derived from the calibrated, range-corrected, and baseline-subtracted lidar return signal. The data have a horizontal resolution ranging from 0.33 km to 5 km and a vertical resolution of 30-300 m depending on altitude. These profiles allow a direct comparison with the simulated aerosol backscatter, offering insight into the vertical structure of the wildfire plume. The CALIPSO data were downloaded from : `https://asdc.larc.nasa.gov/project/CALIPSO/CAL_LID_L1-Standard-V4-51_V4-51`.

To facilitate a direct comparison with the ICON–ART simulations, the CALIPSO overpasses were collocated with the model output in both space and time. For each satellite overpass, the midpoint time of the CALIOP track within the study domain was determined and the closest ICON model output time was selected. The ICON fields were then sampled along the satellite ground track using nearest-neighbour interpolation in the horizontal direction. In order to enable a consistent comparison between the lidar observations and the model output, the CALIOP backscatter profiles were horizontally averaged and interpolated onto a uniform vertical altitude grid before visualization.

4.4.2 MAIAC Aerosol Optical Depth

The Multi-Angle Implementation of Atmospheric Correction (MAIAC) algorithm provides high-resolution aerosol optical depth retrievals based on MODIS Level 1B data [Lyapustin et al., 2012]. MAIAC uses time series analysis combined with pixel- and image-based processing to improve cloud detection, aerosol retrieval, and atmospheric correction. The MODIS L1B radiances (36 bands, 0.4–14.4 μm) are gridded onto a fixed 1 km resolution grid following, enabling consistent observation of the same grid cell over time. By accumulating multi-angle observations over up to 16 days, MAIAC retrieves the surface bidirectional reflectance distribution function (BRDF) and detects both seasonal and rapid surface changes. The MAIAC AOD data used in this study were obtained From: https://ladsweb.modaps.eosdis.nasa.gov/search/order/1/MCD19A2CMG–61

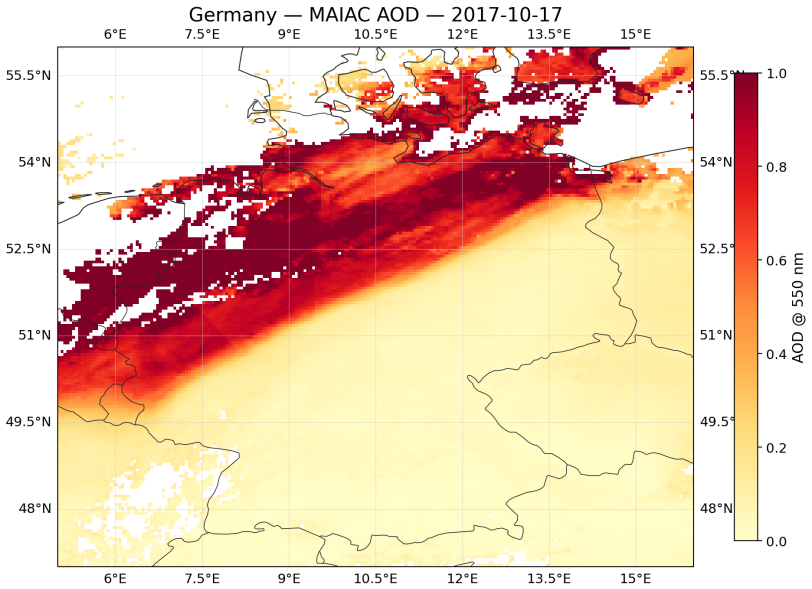

Figure 4.4: MODIS MAIAC aerosol optical depth (AOD) at 550 nm over Germany on 17 October 2017. Enhanced AOD values over northern and central Germany indicate the presence of long-range transported wildfire smoke originating from the Iberian Peninsula. The spatial gradient in AOD highlights the plume extent and its advection across central Europe during this event.

4.4.3 MODIS Cloud Products

Cloud properties used in this study are derived from the Moderate Resolution Imaging Spectroradiometer (MODIS) Level-3 daily product (CLDPROP). This product provides gridded daily composites of cloud fraction (CF) and cloud-top temperature (CTT) on a regular latitude–longitude grid at 1° resolution. The MODIS CLDPROP algorithm retrieves cloud properties using a combination of visible, near-infrared, and infrared channels, enabling consistent global monitoring of cloud macrophysical and microphysical characteristics [Platnick et al., 2016].

For this study, the cloud fraction and cloud-top temperature fields were used to characterize the spatial distribution and thermodynamic structure of clouds over Europe during the October 2017 wildfire event. The analysis combines these MODIS cloud observations with simulated aerosol fields from the ICON-ART model to investigate potential aerosol–cloud interactions.

The MODIS data were obtained from the NASA Level-1 and Atmosphere Archive and Distribution System (LAADS) DAAC. For consistency with the model output, the cloud fields were regridded to match the analysis grid using bilinear interpolation.

5 Results

This chapter evaluates the ability of the ICON-ART simulations to reproduce the October 2017 wildfire event over the Iberian Peninsula by comparing model results with satellite observations. Two complementary datasets are used for validation: aerosol optical depth (AOD) retrievals from the MAIAC algorithm, and attenuated backscatter profiles from the CALIPSO lidar.

The chapter is organized as follows. Section 5.1 presents a comparison of the simulated AOD at 550 nm with MAIAC observations, providing a spatial and temporal assessment of the aerosol load. Section 5.2 then compares the modeled biomass burning aerosol backscatter with CALIPSO attenuated backscatter at 532 nm to evaluate the vertical distribution of the plume. Section 5.3 then examines the statistical relationship between simulated soot AOD and satellite-observed cloud fraction, using a regime-based approach to assess the potential for aerosol-cloud interactions.

5.1 Horizontal Transport of the Plumes

5.1.1 Comparison with ICON-ART Simulations

Figure 5.1 illustrates the spatial evolution of the wildfire smoke plume across Europe during 16–18 October 2017 based on a comparison between MAIAC AOD at 550 nm and ICON-ART simulations performed with and without aerosol-radiation interactions. The ICON-ART simulations reveal a coherent long-range transport pathway originating from the Iberian Peninsula and extending across Western and Central Europe toward Eastern Europe.

On 16 October, pronounced aerosol loading is simulated over the Bay of Biscay and the northeastern Atlantic. MAIAC retrievals appear spatially fragmented due to cloud screening, but enhanced AOD signatures along the plume margins are visible.

On 17 October, the plume is advected eastward across France, the Benelux region, and Germany. MAIAC observations show improved spatial agreement with the simulated plume corridor (Fig. 5.1) compared to the previous day, though the correspondence is not perfect. By 18 October, the plume becomes more aged and diluted while remaining detectable in the ICON-ART simulations over Eastern Europe, whereas MAIAC observations become increasingly sparse due to persistent cloud coverage and reduced clear sky retrieval availability.

A comparison between the ICON-ART experiments shows that the inclusion of aerosol-radiation interactions leads to slightly enhanced plume persistence and spatial coherence, particularly during the early transport phase visible in Figure 5.1.

To enable a direct comparison with the ICON-ART simulations, the MAIAC AOD fields were regridded onto the ICON model grid using the xESMF regridding framework with bilinear interpolation. The MAIAC product represents a daily composite retrieval under clear sky conditions, whereas the ICON fields correspond to instantaneous model output. In this study, the ICON AOD fields closest to 12:00 UTC were used for comparison with the daily MAIAC observations. Because satellite retrievals are only available under clear sky conditions, grid points without valid MAIAC retrievals were excluded and the same spatial mask was applied to the ICON AOD fields to ensure consistent spatial sampling between model and observations.

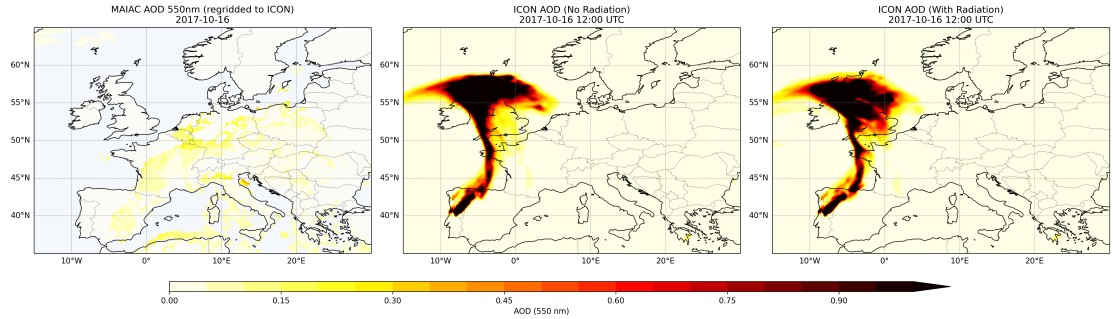

(a) 16 October 2017

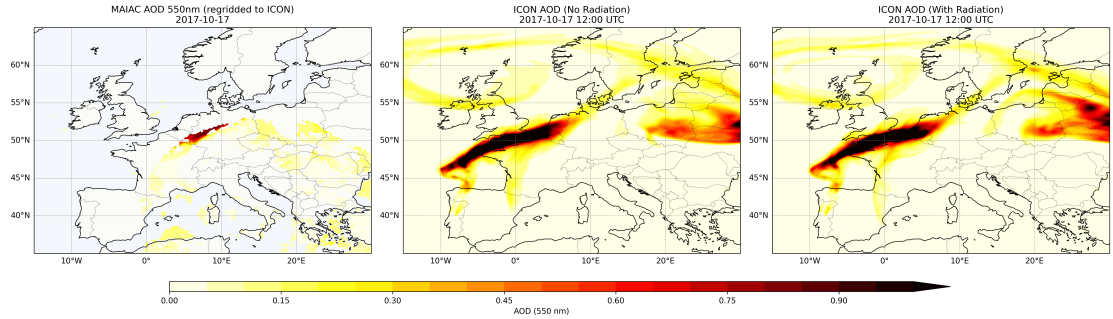

(b) 17 October 2017

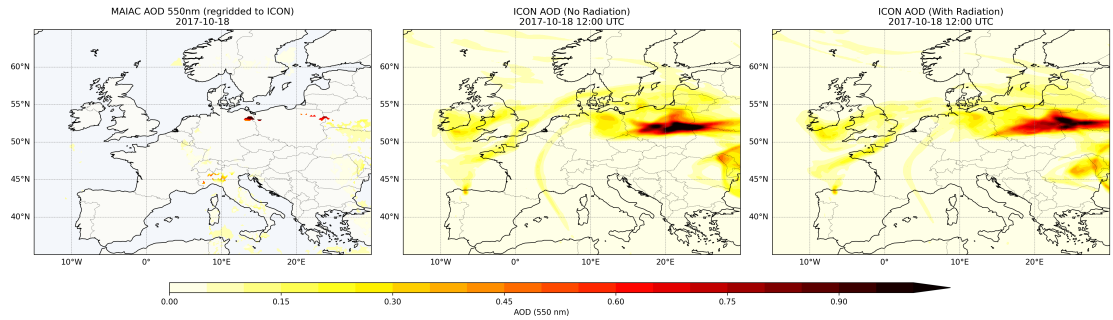

(c) 18 October 2017

Figure 5.1: Spatial distribution of aerosol optical depth (AOD) at 550 nm over Europe during 16–18 October 2017. Each panel compares MODIS MAIAC AOD (regridded to the ICON grid) with ICON-ART simulations with and without aerosol-radiation interactions at 12:00 UTC.

5.2 Vertical Structure and Injection Height

5.2.1 CALIOP-ICON cross-section comparison along satellite overpasses

CALIOP overpasses on 17 and 18 October 2017 provide representative examples of the vertical structure of the transported Iberian wildfire plume over Europe. The CALIOP lidar provides high-resolution vertical profiles of aerosol and cloud layers [Winker et al., 2009]. The horizontal AOD distribution shown in Figure 5.2(a) shows a coherent aerosol

band extending from the Iberian Peninsula toward Central and Northern Europe, with the CALIPSO ground track intersecting the plume corridor. This configuration allows a direct comparison between the satellite lidar observations and the simulated aerosol distribution along the same transect.

The CALIOP attenuated backscatter curtains (Fig. 5.2 (b)) reveal pronounced elevated aerosol layers extending from the lower troposphere up to approximately 10 km altitude. On 17 October, the plume appears as a relatively coherent elevated layer reaching altitudes of roughly 8–11 km along the satellite track. In contrast, the 18 October overpass shows a more fragmented vertical structure with multiple aerosol layers distributed throughout the troposphere.

The corresponding ICON-ART simulated backscatter cross sections (Fig. 5.2 (c)) reproduce the presence and approximate altitude of these elevated aerosol layers. The modeled plume extends through a similar altitude range as observed by CALIOP. However, the modeled layers appear smoother and less sharply defined than in the lidar observations.

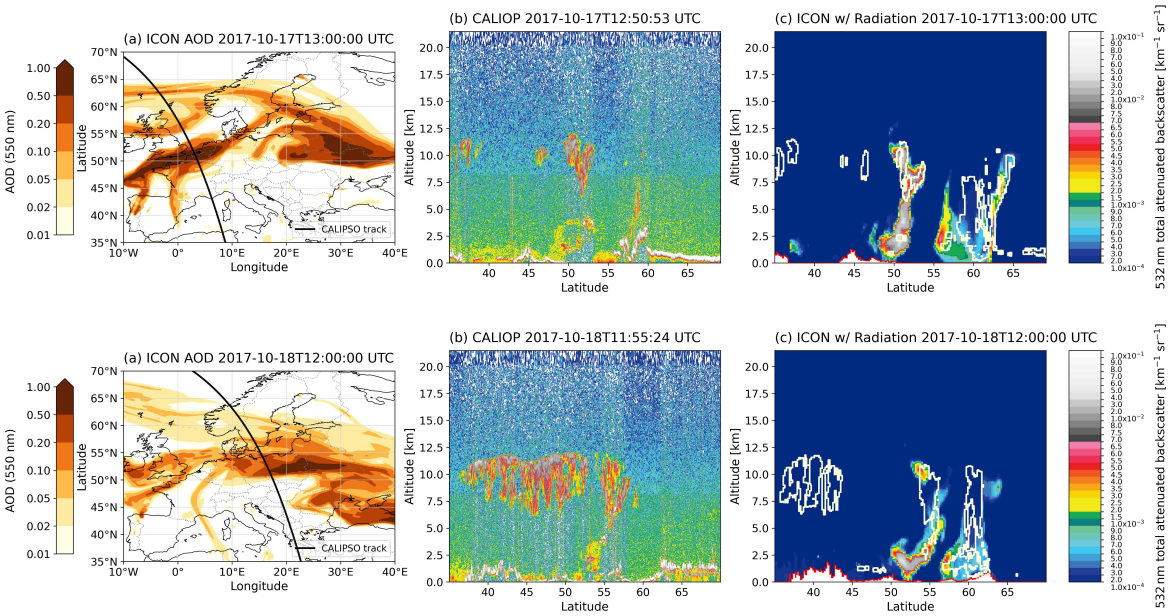

Figure 5.2: Comparison of the vertical structure of the Iberian wildfire plume between CALIOP observations and ICON–ART simulations during two satellite overpasses over Europe. Panels (a) show the simulated soot aerosol optical depth (AOD) at 550 nm together with the CALIPSO ground track. Panels (b) present the CALIOP attenuated backscatter at 532 nm, revealing the vertical distribution of aerosol layers along the satellite track. Panels (c) display the corresponding simulated backscatter from the ICON–ART model including aerosol–radiation interactions.

5.2.2 Sensitivity to aerosol-radiation interactions and fire intensity (SHR factor)

To investigate the sensitivity of the simulated plume structure to key model configuration parameters, two CALIOP overpasses (17 and 18 October 2017) are used as reference cases (Figs. 5.3 and 5.4). The observations are taken from the CALIPSO Level 2 aerosol profile product (APro), in which aerosol layers are first detected by the CALIOP feature-finding scheme and subsequently classified using the CALIOP aerosol subtyping algorithm [Winker et al., 2009, Vaughan et al., 2009, Omar et al., 2009, Kim et al., 2018]. The APro aerosol subtype curtain is a classification mask applied only where an aerosol feature is detected; gaps in the subtype display do not necessarily imply aerosol-free air but may also result from detection limits or signal attenuation beneath optically thick clouds [Winker et al., 2009, Vaughan et al., 2009].

For the 17th October overpass (Fig. 5.3), CALIOP detects aerosol layers along parts of the track, with most subtype retrievals concentrated at low altitudes. Only sparse detections occur in the mid to upper troposphere, and these are primarily classified as dust rather than elevated smoke (subtype 6). The corresponding ICON-ART curtains reproduce the occurrence of elevated aerosol layers along a similar latitude range, although the simulated layers appear more continuous than the sparse subtype detection in the CALIOP product. Differences among the four ICON-ART experiments show variations in the vertical extent and coherence of the simulated backscatter. Increasing the plume-rise scaling from SHR = 3.4 to SHR = 6.8 leads to a higher and more vertically extended plume. Simulations that include aerosol-radiation interactions produce a more coherent and locally slightly higher simulated plume structure compared to the NO-RAD experiments.

The analysis for 18 October 2017 (Fig. 5.4) shows a similar overall behavior, although the CALIOP aerosol subtype detections are sparse. Most retrieved aerosol features are confined to low altitudes, while only isolated pixels appear in the mid to upper troposphere, again predominantly classified as dust rather than elevated smoke. In contrast, the ICON-ART simulations exhibit a coherent and vertically extended plume structure, with elevated aerosol layers reaching altitudes of approximately 8–11 km. Differences among the model configurations remain consistent with the previous day: increasing the plume-rise scaling from SHR = 3.4 to SHR = 6.8 results in higher simulated plume tops, while the inclusion of aerosol–radiation interactions leads to modest but systematic changes in plume coherence and vertical extent.

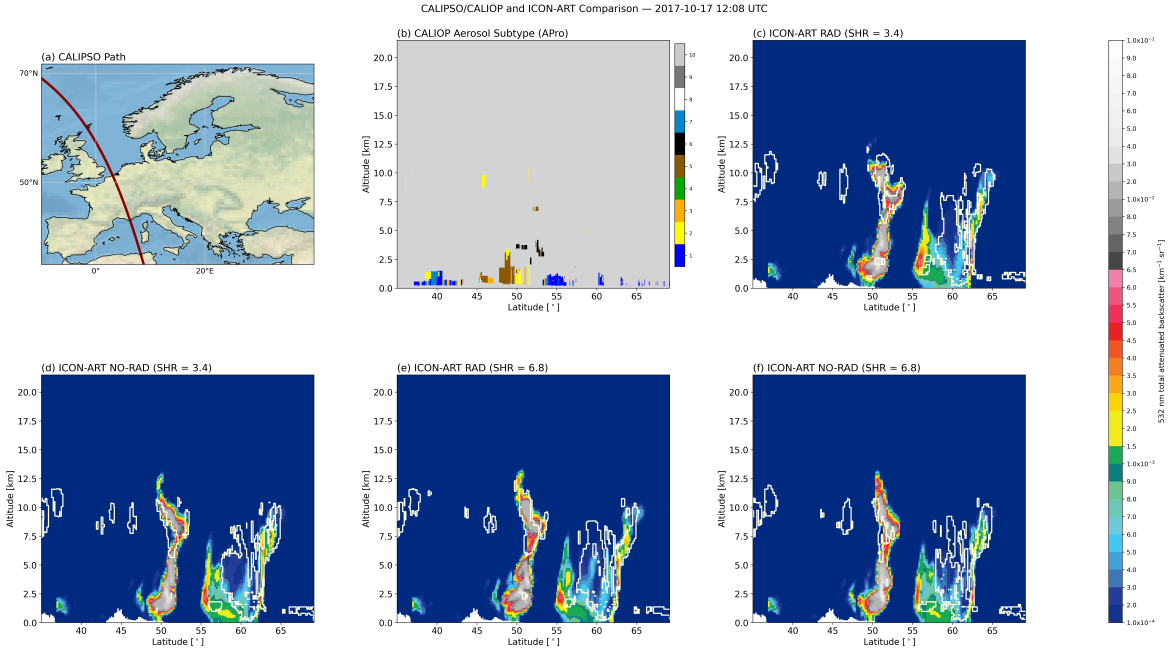

Figure 5.3: Sensitivity of the simulated vertical plume structure to aerosol-radiation interactions and fire intensity during the CALIOP overpass on 17 October 2017 at 12:08 UTC. Panel (a) shows the CALIPSO ground track across Europe. Panel (b) presents the CALIOP aerosol subtype classification from the Level 2 aerosol profile product (APro) [Omar et al., 2009, Kim et al., 2018]. The subtype categories correspond to: 1 = marine, 2 = dust, 3 = polluted continental/smoke, 4 = clean continental, 5 = polluted dust, 6 = elevated smoke, 7 = dusty marine, 8 = PSC aerosol, 9 = volcanic ash, and 10 = sulfate/other [Kim et al., 2018]. Panels (c)-(f) show ICON–ART simulated 532 nm attenuated backscatter along the same track for four model configurations: with aerosol–radiation interactions and SHR = 3.4 (c), without radiation and SHR = 3.4 (d), with radiation and SHR = 6.8 (e), and without radiation and SHR = 6.8 (f). White contours indicate simulated cloud layers based on the sum of cloud liquid and ice water content.

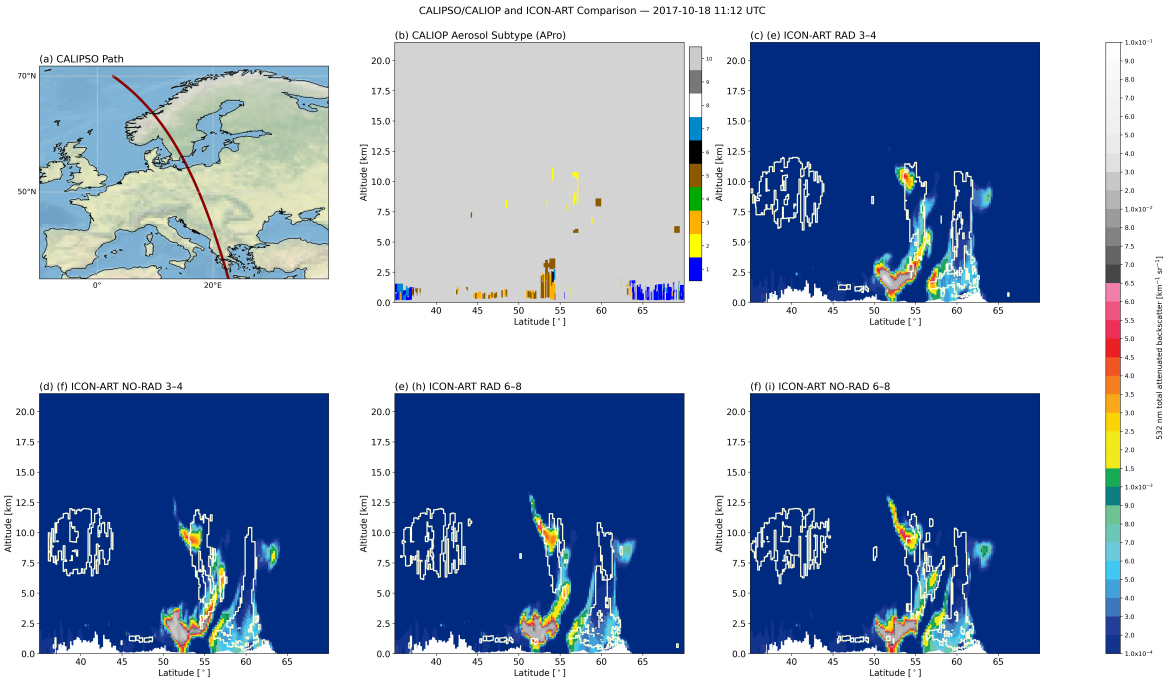

Figure 5.4: Same as Fig. 5.3, but for the CALIOP overpass on 18 October 2017. Subtype definitions follow Kim et al. [2018].

5.3 Statistical Aerosol–Cloud Relationship

To explore potential relationships between transported wildfire aerosol and cloud properties, a statistical analysis of aerosol optical depth (AOD) and cloud fraction (CF) was performed. Both datasets were spatially matched by regridding the model AOD field onto the MODIS grid using bilinear interpolation. The analysis was restricted to the European domain defined by 35°–65° N and 15° W–30° E, covering the main transport pathway of Iberian wildfire plumes. The analysis covers the period 13–18 October 2017, during which the smoke plume from the Iberian wildfires was transported across large parts of Europe.

To reduce ambiguity caused by intermediate aerosol and cloud conditions, a regime classification approach was adopted. Grid cells were divided into four distinct regimes based on threshold values for AOD and cloud fraction. Pixels with AOD ≤ 0.2 were classified as *clean*, while pixels with AOD ≥ 0.4 were classified as *polluted*. Similarly, pixels with cloud fraction ≤ 0.2 were defined as *clear*, whereas pixels with cloud fraction ≥ 0.8 were categorized as *cloudy*. Pixels with intermediate values were excluded from the statistical analysis in order to ensure well separated aerosol and cloud regimes.

This classification yields four aerosol-cloud regimes:

- Clear and clean conditions (AOD ≤ 0.2, CF ≤ 0.2)
- Clear and polluted conditions (AOD ≥ 0.4, CF ≤ 0.2)

- Cloudy and clean conditions (AOD ≤ 0.2, CF ≥ 0.8)
- Cloudy and polluted conditions (AOD ≥ 0.4, CF ≥ 0.8)

Figure 5.5 shows the spatial distribution of these regimes over Europe for 17 October 2017. Cloudy and clean conditions dominate northern Europe. Clearer conditions occur mainly over southern Europe and the Mediterranean region. Regions classified as polluted appear primarily along the pathway of the transported smoke plume originating from the Iberian Peninsula.

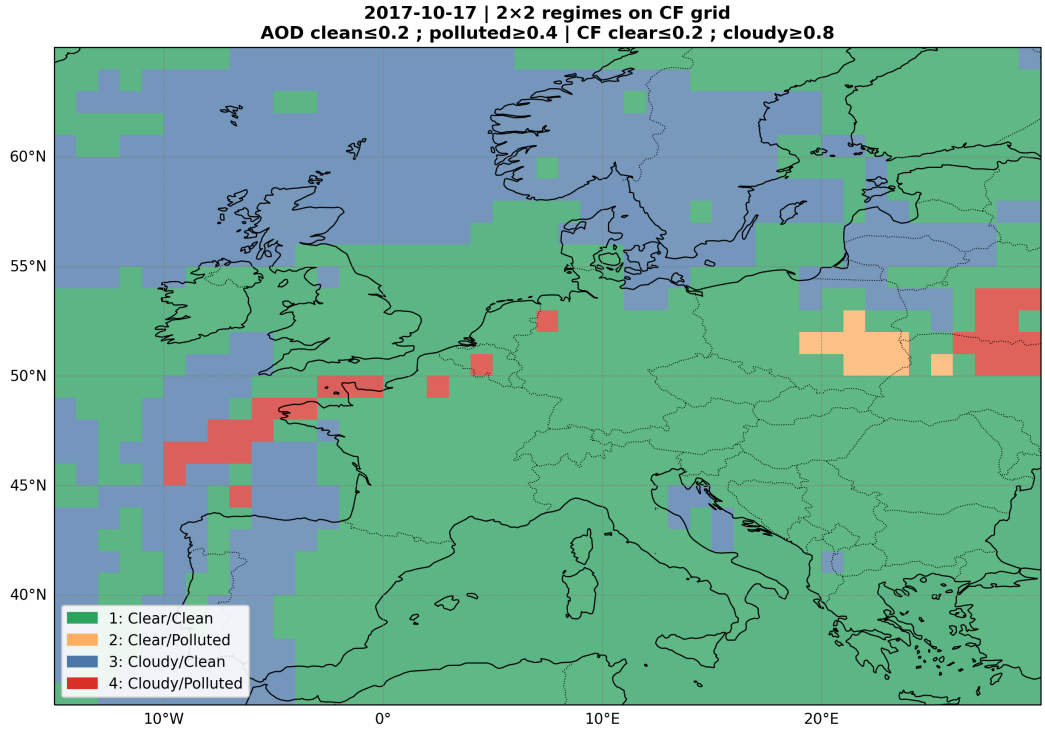

Figure 5.5: Spatial distribution of aerosol-cloud regimes over Europe on 17 October 2017. Regimes are defined using AOD thresholds (clean ≤ 0.2, polluted ≥ 0.4) and cloud fraction thresholds (clear ≤ 0.2, cloudy ≥ 0.8). Only grid cells meeting these criteria are shown.

To quantify the relationship between aerosol loading and cloud fraction, scatter plots were constructed and Pearson correlation coefficients were calculated for the different regimes. Figure 5.6 presents the combined scatter plot of ICON soot AOD at 550 nm and MODIS cloud fraction for all regimes included in the analysis.

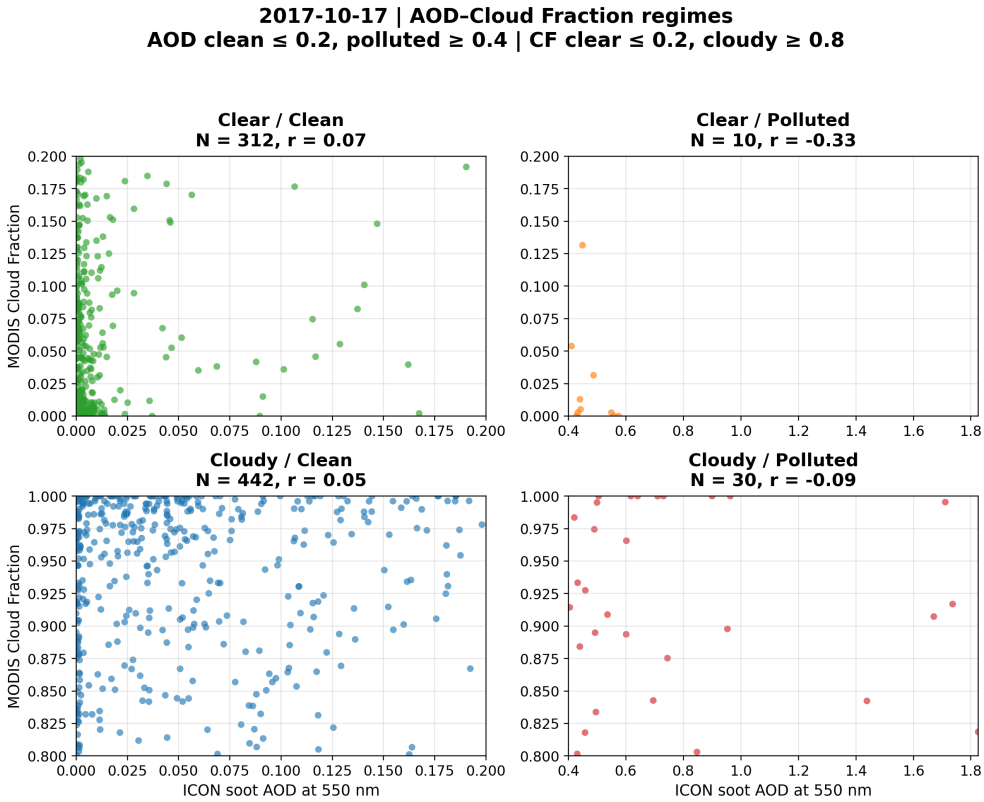

Figure 5.6: Relationship between ICON soot AOD at 550 nm and MODIS cloud fraction for the four aerosol–cloud regimes defined in this study. Colors represent the four regimes: clear–clean, clear–polluted, cloudy–clean, and cloudy–polluted conditions.

Table 5.1 summarizes the number of grid cells and the correlation coefficients between AOD and cloud fraction for each regime.

Table 5.1: Statistical summary of aerosol–cloud regimes for 17 October 2017.

Regime	Number of Pixels	Correlation (r)
Clear–Clean	312	0.07
Clear–Polluted	10	-0.33
Cloudy–Clean	442	0.05
Cloudy–Polluted	30	-0.09
All regimes combined	794	0.19

The polluted-cloudy regime has relatively few pixels, with 30 pixels in the cloudy-polluted regime an 10 pixels in the clear-polluted regime. Therefore, the corresponding correlations should be interpreted with caution.

5.3.1 18 October 2017

The same regime classification was examined for 18 October 2017. By this time the transported wildfire plume had moved further east across Europe, while extensive cloud systems remained present over large parts of the continent.

Figure 5.7 shows the spatial distribution of the aerosol–cloud regimes on 18 October. Compared to the previous day, the polluted pixels appear further downstream along the transport pathway of the plume. The majority of cloudy grid cells remain classified as clean.

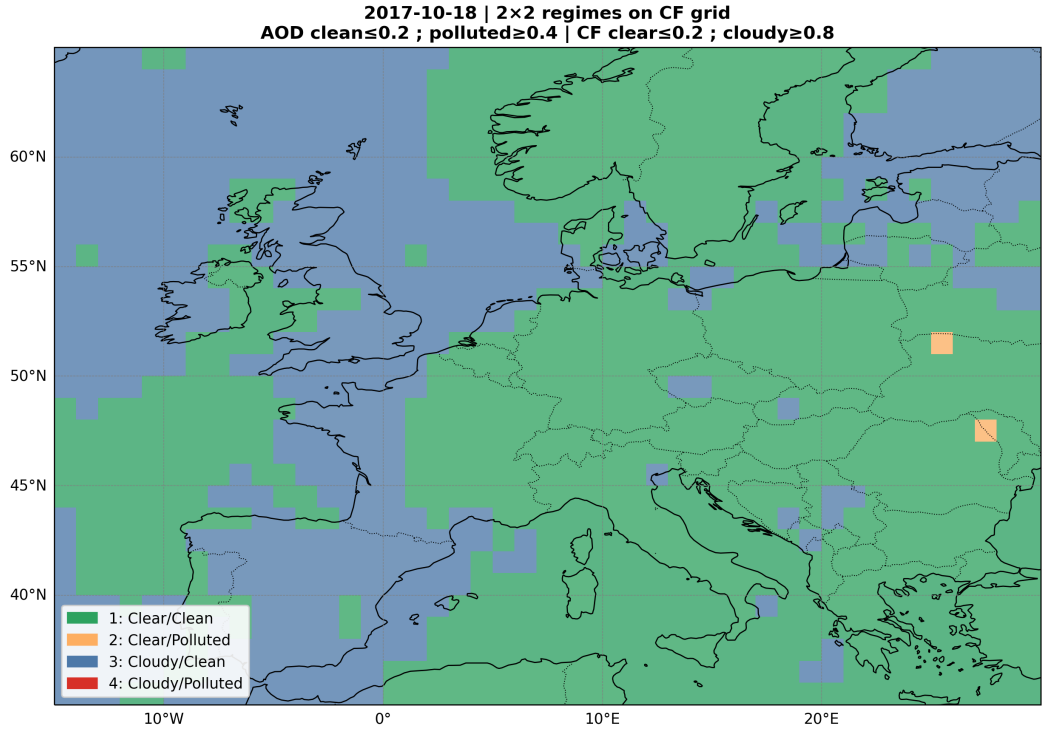

Figure 5.7: Spatial distribution of aerosol–cloud regimes over Europe on 18 October 2017 using the same classification thresholds as in Fig. 5.5.

The corresponding scatter relationship between ICON soot AOD and MODIS cloud fraction is shown in Fig. 5.8. The data points cluster primarily within the clear-clean and cloudy-clean regimes, while polluted regimes contain only a small number of pixels.

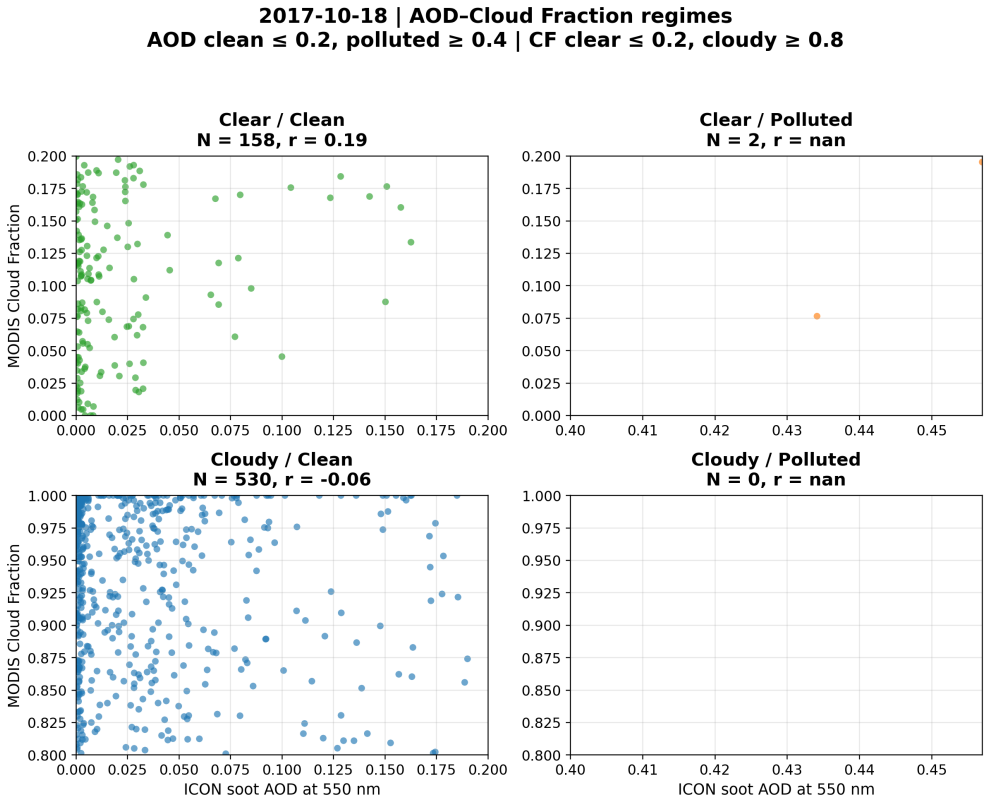

Figure 5.8: Relationship between ICON soot AOD at 550 nm and MODIS cloud fraction for 18 October 2017.

5.3.2 Regime-dependent cloud-fraction differences in plume-affected regions

To further investigate whether the spatial co-occurrence of transported wildfire smoke and cloud fields is associated with systematic changes in cloud properties, a regime-dependent analysis of cloud fraction (CF) was performed. Cloud regimes were defined based on MODIS cloud-top temperature (CTT), separating warm, mixed-phase, and cold cloud conditions. For each regime, grid cells were classified as plume-affected using the ICON-ART plume mask combined with regime-specific plume-top height thresholds.

For each day, the mean cloud fraction in plume-affected grid cells (CF_{plume}) was compared to the mean cloud fraction in non-plume grid cells (CF_{bg}) of the same regime, and the difference $\Delta CF = CF_{plume} - CF_{bg}$ was calculated.

Figure 5.9 illustrates the spatial configuration on 17 October 2017. The plume is transported as a coherent and elevated layer across western and central Europe, while cloud occurrence and thermodynamic structure exhibit strong spatial variability.

The resulting daily ΔCF values are shown in Table 5.2. In the warm regime, ΔCF ranges from negative values (e.g., -0.30 on 15 October) to positive values (e.g., $+0.37$ on 18 October). In the mixed-phase regime, a large negative anomaly is observed on 15 October ($\Delta CF \approx -0.37$),

followed by smaller positive values on subsequent days. The cold-cloud regime exhibits ΔCF values close to zero on most days.

Table 5.2: Daily cloud fraction (CF) in plume-affected (p) and background (b) regions, and their difference (ΔCF), for different cloud regimes.

	Warm			Mixed			Cold		
Date	CF_p	CF_b	ΔCF	CF_p	CF_b	ΔCF	CF_p	CF_b	ΔCF
14/10	0.402	0.694	-0.292	–	0.770	–	–	0.956	–
15/10	0.311	0.612	-0.301	0.500	0.872	-0.372	0.872	0.978	-0.106
16/10	0.793	0.521	0.272	0.887	0.849	0.038	0.998	0.985	0.013
17/10	0.439	0.596	-0.156	0.944	0.905	0.039	1.000	0.990	0.009
18/10	0.890	0.519	0.371	0.952	0.877	0.075	0.996	0.991	0.004

5.3.3 Plume–Cloud Interaction Geometry

To better understand the spatial relationship between the transported wildfire plume and cloud fields, the daily plume diagnostics from ICON-ART were combined with MODIS cloud observations. While the statistical analysis in the previous section relied on aerosol optical depth and cloud fraction, the present analysis focuses on the geometric overlap between the simulated smoke plume and observed cloud regimes.

These variables describe the spatial distribution and thermodynamic structure of the cloud field over Europe. In parallel, the ICON-ART simulations provide information on the vertical distribution of the wildfire plume. From the model output, the daily maximum plume-top height and a daily plume presence mask were derived. A grid cell was classified as plume-affected if the column-integrated soot AOD exceeded a threshold value at any model output time during that day.

To allow a direct comparison with the MODIS observations, the ICON plume-top height and plume mask were regridded to the MODIS grid. This makes it possible to examine where elevated smoke layers and different cloud regimes occur simultaneously.

Figure 5.9 illustrates the plume-cloud geometry over Europe on 17 October 2017. Panel (a) shows the MODIS cloud-top temperature field, panel (b) shows the MODIS cloud fraction, panel (c) shows the regridded ICON plume-top height, and panel (d) shows a mask highlighting grid cells where cold-cloud conditions (CTT < 258 K) coincide with elevated plume tops (plume-top height > 8 km).

The cloud fraction field reveals widespread cloud cover over northern and central Europe, while lower cloud fractions occur mainly over southern Europe and parts of the Mediterranean. The ICON plume-top heights indicate that the wildfire smoke plume is transported as an elevated layer, reaching several kilometers into the free troposphere across large parts of western and central Europe.

The combined cold-high-plume mask highlights regions where an overlap between cold-cloud conditions and elevated smoke layers is geometrically possible.

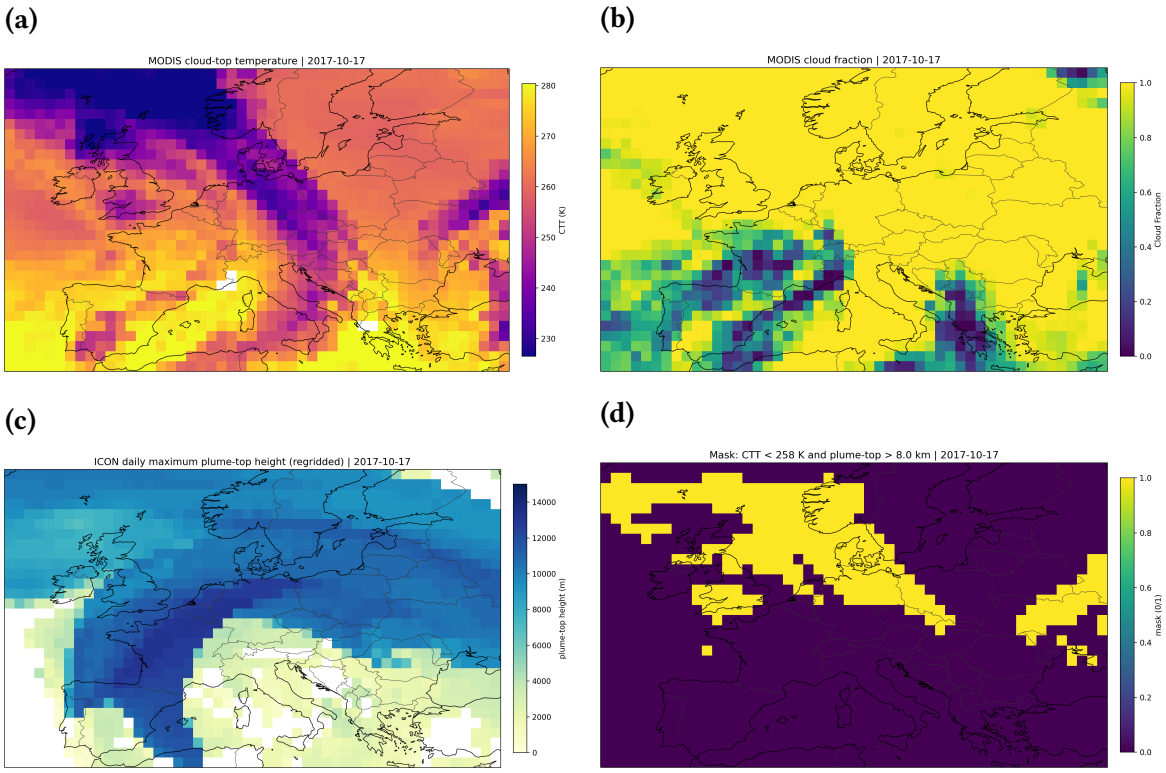

Figure 5.9: Plume–cloud interaction geometry over Europe on 17 October 2017. (a) MODIS cloud-top temperature (CTT). (b) MODIS cloud fraction (CF). (c) Daily maximum plume-top height simulated by ICON-ART and regridded to the MODIS grid. (d) Mask of grid cells where cold-cloud conditions (CTT < 258 K) coincide with elevated plume tops (plume-top height > 8 km).

6 Discussion

6.1 Interpretation of Key Findings

The statistical analysis presented in Section 5.3 revealed only a weak overall correlation between aerosol optical depth (AOD) and cloud fraction (CF) during the October 2017 wildfire event, with only 30 pixels (less than 4% of the domain) falling into the polluted-cloudy regime. The geometric analysis further showed that the smoke plume was predominantly elevated in the upper troposphere, reaching 8–11 km altitude, while extensive cloud cover was located mainly over northern Europe, leading to a pronounced spatial separation. These findings suggest that column-integrated AOD alone is insufficient to capture potential aerosol effects on clouds. The following subsections interpret these results in light of process based mechanisms and highlight the factors that limit direct aerosol-cloud interactions in this event.

6.1.1 The Role of Vertical Distribution

A key limitation of using AOD as a proxy for aerosol-cloud interactions is that it integrates over the entire atmospheric column, providing no information on the altitude of aerosol layers relative to cloud layers. As demonstrated by the CALIPSO curtains in Section 5.2, the smoke plume during the October 2017 event was predominantly elevated in the upper troposphere, limiting direct interaction with lower cloud layers. Clouds forming below this layer such as boundary layer stratocumulus — were physically separated from the aerosol, preventing direct microphysical interactions.

This finding is consistent with Dong et al. [2024], who explicitly note that "if the smoke occurs only above the low clouds and does not make any contact with them, it cannot serve as CCN and thus will not influence the cloud properties." In their study of the 2020 Western United States wildfires, smoke was present both above and below stratocumulus clouds, allowing it to mix into cloud layers and significantly enhance cloud water. The contrast with our case highlights that vertical overlap is a necessary condition for aerosol microphysical effects.

6.1.2 Aerosol Composition and CCN Activity

Even when vertical overlap occurs, the ability of aerosols to influence clouds depends on their composition and aging state. Biomass burning aerosols contain a mixture of black

carbon (BC) and organic carbon (Organic Carbon (OC)), with BC being hydrophobic and relatively ineffective as cloud condensation nuclei (CCN) unless aged and coated with soluble material [Samset et al., 2018]. During transport, aging processes modify particle morphology, hygroscopicity, and mixing state, but these transformations take time and depend on atmospheric conditions.

Smith et al. [2018] demonstrated that black carbon produces strong negative rapid adjustments, with the largest contributions from tropospheric temperature and cloud changes. Importantly, these adjustments depend critically on the vertical and horizontal distribution of the aerosol a column integrated measure like AOD cannot capture them. In the October 2017 event, the transported smoke may not have undergone sufficient aging to become efficient CCN, further limiting its potential to modify cloud properties.

6.1.3 Observational Limitations

Satellite-based aerosol retrievals are often unavailable in regions with extensive cloud cover. This sampling limitation introduces a systematic bias in observational datasets, as aerosol retrievals are preferentially obtained under cloud free conditions. Consequently, correlations between AOD and cloud properties can be strongly influenced by meteorological covariability rather than by direct aerosol effects [Gryspeerdt et al., 2016]. In particular, large-scale atmospheric circulation patterns and humidity fields frequently dominate cloud formation processes, masking potential aerosol influences.

In the October 2017 event, the smoke was transported in dry, subsiding air masses associated with the passage of ex-hurricane Ophelia, while cloudy regions were located in moister environments over northern Europe [Ramos et al., 2023]. The spatial separation of smoke and moisture regimes captured by the regime maps in Section 5.3 meant that even if the smoke had been capable of acting as CCN, the necessary moisture for cloud formation was not colocated with the aerosol.

6.1.4 The Semi-Direct Effect and Context Dependence

Absorbing aerosol components such as black carbon can influence clouds through aerosol-radiation interactions rather than purely through microphysical aerosol-cloud interactions. The absorption of solar radiation by black carbon heats the surrounding air and modifies atmospheric stability, which can alter cloud formation indirectly through the so-called semi-direct effect [Tegen and Heinold, 2018]. Such radiative effects depend strongly on the vertical position of aerosol layers and therefore cannot be captured by AOD alone.

The influence of aerosols on clouds is not universal the same aerosol type can have opposing effects depending on meteorological context. Ding et al. [2021] showed that biomass burning smoke reduces cloudiness in the Amazon through surface cooling and reduced relative humidity (the classic semi-direct effect), yet enhances low clouds over the southeast Atlantic

and subtropical Asia when it resides above the cloud layer and creates a strong inversion. This context-dependence further reinforces the inadequacy of AOD as a standalone metric.

6.1.5 Toward a More Comprehensive Approach

These considerations suggest that interpreting aerosol-cloud relationships requires additional information beyond column aerosol loading. In particular, vertically resolved observations, such as lidar measurements from the CALIPSO satellite, together with numerical simulations from models such as ICON-ART, provide important constraints on aerosol layer altitude and radiative effects. Combining these approaches allows a more comprehensive assessment of how transported wildfire smoke modifies atmospheric structure and cloud formation processes.

Table 6.1 summarizes the key mechanisms by which black carbon can influence clouds, including both microphysical (ACI) and radiative (ARI, semi-direct effect) pathways [Boucher et al., 2013, Ohneiser et al., 2023, Tegen and Heinold, 2018].

Table 6.1: Summary of key mechanisms linking black carbon to cloud processes.

Mechanism	Description	Atmospheric effect
Aerosol–Cloud Interaction (ACI)	Aerosol particles act as cloud condensation nuclei and modify droplet number and size	Increased droplet number, smaller droplets, higher cloud albedo
Aerosol–Radiation Interaction (ARI)	Absorption of solar radiation by black carbon heats the surrounding air	Atmospheric warming and modified stability
Semi-direct effect	Heating by absorbing aerosols leads to evaporation or suppression of clouds	Reduction of cloud cover under some conditions
Self-lofting	Absorption increases buoyancy of aerosol layers	Upward transport of smoke plumes

6.1.6 Summary

In summary, the weak correlation between AOD and cloud fraction observed during the October 2017 wildfire event reflects:

- **Vertical separation** between the elevated smoke plume and cloud layers [Dong et al., 2024]
- **Limited horizontal overlap** due to contrasting meteorological regimes
- **Aerosol composition and aging** that limit CCN activity [Samset et al., 2018, Smith et al., 2018]

- **Observational limitations** including cloud screening and retrieval biases [Gryspeerdt et al., 2016]
- The inherent **context-dependence** of aerosol-cloud interactions [Ding et al., 2021]

These factors collectively demonstrate that column-integrated AOD alone is an insufficient proxy for aerosol effects on clouds. Vertically resolved information, aerosol composition, and meteorological context must all be considered a conclusion that is strongly supported by the growing body of literature on this topic.

6.2 Model Performance in Simulating Plume Transport and Vertical Structure

The evaluation of ICON-ART against MAIAC AOD and CALIPSO observations (Sections 5.1 and 5.2) showed that the model successfully reproduced the large-scale transport of the smoke plume across Europe and its elevated vertical structure, with injection heights reaching 8–11 km on 17 October. The inclusion of aerosol-radiation interactions led to slightly enhanced plume persistence and spatial coherence, consistent with the radiative heating effects of absorbing aerosols [Boucher et al., 2013, Ohneiser et al., 2023].

Sensitivity experiments demonstrated that both aerosol-radiation interactions and the fire intensity scaling factor (SHR) influenced the simulated plume height and vertical extent. Increasing SHR from 3.4 to 6.8 resulted in a higher and more vertically extended plume, in agreement with the known dependence of plume rise on fire heat release [Freitas et al., 2007, Paugam et al., 2016]. However, the simulation with SHR = 3.4, which corresponds to the standard GFAS enhancement factor, produced plume heights that best matched the CALIPSO observations (8–11 km), whereas SHR = 6.8 led to an overestimation of the plume top. This sensitivity highlights the importance of accurate fire intensity data for plume-rise parameterizations.

The close agreement between the model and observations SHR = 3.4 supports the first hypothesis that ICON-ART can realistically capture the injection height and transport of wildfire emissions under extreme conditions. However, some discrepancies remained, such as the smoother simulated backscatter curtains compared to the sharp CALIOP features. These are expected due to the model's coarser resolution and numerical diffusion [Schröter et al., 2018]. Overall, the model validation confirms that ICON-ART is a suitable tool for studying the long-range transport of wildfire smoke.

6.3 Comparison with Previous Studies

6.3.1 Limitations of AOD as a Proxy

The finding that column-integrated AOD is a poor indicator of aerosol–cloud interactions is consistent with previous studies that highlighted the limitations of using AOD alone. For instance, Stier [2016] showed that the correlation between AOD and CCN concentrations is relatively low over large parts of the globe, indicating that AOD does not reliably represent the aerosol particles that actively participate in cloud formation. Similarly, Gryspeerdt et al. [2016] demonstrated that sampling biases in satellite aerosol retrievals (preferentially obtained under cloud-free conditions) can lead to spurious correlations that are dominated by meteorological covariability rather than direct aerosol effects.

6.3.2 Comparison with ICON-ART Wildfire Studies

Muth et al. [2025] investigated the Australian Black Summer Fires (2019/2020) using the same ICON-ART framework, providing a valuable point of comparison for the present study. Consistent with this study, they demonstrated that including fire-induced heat release significantly increased plume height due to enhanced buoyancy, while moisture release had minimal impact on plume dynamics [Muth et al., 2025]. Similar to the SHR sensitivity experiments of the present study, they found that higher fire intensity produced more vertically extended plumes.

Regarding aerosol-radiation interactions, Muth et al. [2025] observed an initial reduction in injection height due to atmospheric stabilization by absorbing aerosols, followed by a lofting effect from the second day onward a pattern consistent with the self-lofting mechanism discussed in Section 2.2.3. The relative position of aerosol and clouds was identified as critical: lofting was strongest when aerosols were positioned above optically thick clouds. This supports our geometric analysis, which emphasized that vertical overlap between smoke and clouds is essential for understanding aerosol effects.

The combined experiment of Muth et al. [2025] (heat + moisture + ARI) produced the highest plume rise (18 km) and best matched CALIOP observations, with average plume tops of 8.6 km. Importantly, they concluded that for small to moderate fires, fire-atmosphere feedbacks can be neglected, but for extreme events such as the October 2017 Iberian wildfires, these effects are crucial. This validates this study focus on an extreme event and the inclusion of ARI and sensible heat release in our simulations.

7 Conclusion

7.1 Summary of Main Findings

This thesis addressed two research questions. The first question asked: *How accurately can ICON-ART simulate the injection height, long-range transport, and vertical distribution of aerosols emitted during the October 2017 wildfires when evaluated against MODIS and CALIOP observations?*

The comparison with satellite observations yielded the following key results:

- **Horizontal transport:** ICON-ART successfully reproduced the large-scale transport of the smoke plume from the Iberian Peninsula across Western and Central Europe. The model captured the spatial evolution of the plume between 16 and 18 October 2017 (the main transport phase of the event), with the inclusion of aerosol-radiation interactions leading to slightly enhanced plume persistence and spatial coherence. Discrepancies with MAIAC AOD were primarily attributable to observational sampling limitations (cloud screening) rather than deficiencies in modeled transport.
- **Vertical structure and injection height:** The comparison with CALIOP lidar observations demonstrated that ICON-ART realistically represents the vertical distribution of the wildfire plume. The model captured the elevated nature of the smoke layer, with injection heights reaching 8–11 km on 17 October and a more fragmented structure on 18 October. Sensitivity experiments showed that both the representation of aerosol-radiation interactions and the fire intensity scaling factor (SHR) influence the simulated plume height and vertical extent. Increasing SHR from 3.4 to 6.8 resulted in a higher and more vertically extended plume, consistent with the known dependence of plume rise on fire heat release. The simulation with SHR = 3.4 (the standard GFAS enhancement factor) produced plume heights that best matched the observations, whereas SHR = 6.8 overestimated the plume top.

Answer to Research Question 1: ICON-ART successfully reproduced the observed injection heights and transport patterns. Minor differences between the simulated and observed fields can be attributed to model resolution, numerical diffusion, and the use of Integrated Forecasting System (IFS) initial conditions (DWD operational analyses for 2017 introduced a spatial shift and were therefore not used). In recent years, simulations with DWD initial data have shown improved agreement, highlighting the sensitivity to the quality of meteorological initialisation.

The second research question asked: *To what extent did the transported smoke plume influence radiative conditions and aerosol-cloud interactions over downwind regions such as Germany?*

The analysis yielded the following insights:

- **Statistical aerosol-cloud relationship:** A regime-based analysis of ICON soot AOD and MODIS cloud fraction revealed only a weak overall correlation ($r = 0.19$ for all valid pixels on 17 October). The most striking finding was the extremely limited spatial overlap between heavy smoke (AOD ≥ 0.4) and extensive cloud cover (cloud fraction ≥ 0.8): on 17 October, only 30 pixels (less than 4% of the domain) fell into the polluted-cloudy regime, and the correlation in this regime was negligible ($r = -0.09$). The same pattern was observed on 18 October, confirming the robustness of this result.
- **Geometric plume-cloud overlap:** The analysis of daily plume-top heights and MODIS cloud regimes further illustrated that the smoke plume was predominantly elevated (several kilometers above the surface) and often located in regions with different cloud thermodynamic structures. Cold clouds (CTT < 258 K) were primarily situated north of the main plume axis, while the smoke overlapped mainly with mid-level and warm clouds. This geometric configuration limits the potential for direct aerosol–cloud interactions and explains why column-integrated AOD alone is insufficient to capture such effects.

Answer to Research Question 2: The transported smoke showed very limited spatial overlap with clouds (only 30 pixels in the polluted-cloudy regime), indicating that column AOD alone cannot explain aerosol effects on clouds. Any potential influence would be restricted to specific regions where elevated smoke coincides with mid-level clouds.

7.2 Implications and Contributions

The findings of this thesis have several implications for the modeling and observational assessment of wildfire smoke and its interactions with clouds:

- ICON-ART realistically simulates injection height and long-range transport of wildfire emissions, supporting its use for forecasting and process studies. The sensitivity to SHR underscores the importance of accurate fire intensity data for plume-rise parameterisations.
- The weak correlation between AOD and cloud fraction and the limited spatial overlap between smoke and clouds highlight that column-integrated AOD is an unreliable proxy for aerosol effects on clouds in elevated smoke plumes.
- The geometric analysis demonstrates the necessity of vertically resolved information for assessing aerosol–cloud interactions. Combining CALIPSO observations with ICON-ART simulations provides a framework to diagnose actual plume-cloud overlap.

7.3 Limitations and Outlook

While this study provides a comprehensive evaluation of the October 2017 wildfire event, several limitations should be acknowledged. First, the analysis is based on a single case study; generalisation to other fire episodes requires multi-event investigations. Second, the model simulations were performed at a horizontal resolution of approximately 26 km, which may not resolve small-scale processes influencing plume development and cloud interactions. Third, the statistical analysis was limited to cloud fraction; other cloud properties (e.g., droplet effective radius, cloud-top temperature, liquid water path) may respond differently to aerosol perturbations.

Future research should address these limitations through the following directions:

- Extend the analysis to multiple wildfire events across different regions and seasons to assess the robustness of the findings.
- Investigate the sensitivity of aerosol-cloud interactions to model resolution by performing simulations at finer grid spacing.
- Incorporate additional satellite products, such as cloud droplet effective radius from MODIS or radar-lidar combinations from CALIPSO, to provide a more complete picture of cloud microphysical responses.
- Explore the role of aerosol aging and composition by including more detailed aerosol chemistry schemes in ICON-ART, which could modify the hygroscopicity and CCN activity of smoke particles.
- Develop diagnostic metrics that account for the vertical profile of aerosols (e.g., using simulated or observed aerosol layer height) when evaluating aerosol-cloud interactions in models and observations.

Accurate simulation of wildfire emissions, transport, and aerosol-cloud interactions is not only of scientific interest but also directly relevant for operational weather and climate forecasts, which support decision making across multiple sectors.

In conclusion, this thesis demonstrates that ICON-ART is a valuable tool for simulating the transport and vertical distribution of wildfire smoke, but also highlights that the assessment of aerosol-cloud interactions requires more than column integrated aerosol optical depth. The findings contribute to a better understanding of the processes governing the atmospheric impacts of extreme wildfire events and provide a foundation for future observational and modeling studies.

Bibliography

Adeyemi A Adebiyi, Paquita Zuidema, and Steven J Abel. The convolution of dynamics and moisture with the presence of shortwave absorbing aerosols over the southeast atlantic. *Journal of Climate*, 28(5):1997–2024, 2015.

SK Akagi, Robert J Yokelson, Christine Wiedinmyer, Matthew J Alvarado, Jeffery S Reid, Thomas Karl, John D Crounse, and Paul O Wennberg. Emission factors for open and domestic biomass burning for use in atmospheric models. *Atmospheric Chemistry and Physics*, 11(9):4039–4072, 2011.

Bruce A Albrecht. Aerosols, cloud microphysics, and fractional cloudiness. *Science*, 245 (4923):1227–1230, 1989.

N Andela, JW Kaiser, GR Van Der Werf, and MJ Wooster. New fire diurnal cycle characterizations to improve fire radiative energy assessments made from modis observations. *Atmospheric Chemistry and Physics*, 15(15):8831–8846, 2015.

Hendrik Andersen. *A quantitative, satellite-based analysis of aerosol effects on liquid-water clouds*. doctoralthesis, Ruhr-Universität Bochum, Universitätsbibliothek, 2017.

Meinrat O Andreae and A Gelencsér. Black carbon or brown carbon? the nature of light-absorbing carbonaceous aerosols. *Atmospheric Chemistry and Physics*, 6(10):3131–3148, 2006.

MO Andreae. Global change, atmospheric chemistry, and the biosphere. *Geosphere-Biosphere Interactions and Climate*, page 15, 2001.

Sofia Augusto, Nuno Ratola, Patricia Tarín-Carrasco, Pedro Jiménez-Guerrero, Marco Turco, Marta Schuhmacher, Solange Costa, JP Teixeira, and Carla Costa. Population exposure to particulate-matter and related mortality due to the portuguese wildfires in october 2017 driven by storm ophelia. *Environment International*, 144:106056, 2020.

Tami C Bond, Sarah J Doherty, David W Fahey, Piers M Forster, Terje Berntsen, Benjamin J DeAngelo, Mark G Flanner, Steven Ghan, Bernd Kärcher, Dorothy Koch, et al. Bounding the role of black carbon in the climate system: A scientific assessment. *Journal of geophysical research: Atmospheres*, 118(11):5380–5552, 2013.

Oea Boucher, D Randall, P Artaxo, C Bretherton, G Feingold, P Forster, VM Kerminen, Y Kondo, H Liao, U Lohmann, et al. Climate change 2013: the physical science basis. contribution of working group i to the fifth assessment report of the intergovernmental panel on climate change. *K., Tignor, M., Allen, SK, Boschung, J., Nauels, A., Xia, Y., Bex, V., and Midgley, PM, Cambridge University Press, Cambridge, UK*, 10, 2013.

Olivier Boucher. Atmospheric aerosols. In *Atmospheric Aerosols: Properties and Climate Impacts*, pages 9–24. Springer, 2015.

Michalina Broda, Olga Zawadzka-Mańko, Krzysztof Markowicz, Peng Xian, and Edward Hyer. A novel framework for assessing regional wildfires contributions to biomass burning aerosol optical depth. *Atmospheric Chemistry and Physics*, 25(20):14015–14043, 2025.

Hunter Brown, Xiaohong Liu, Rudra Pokhrel, Shane Murphy, Zheng Lu, Rawad Saleh, Tero Mielonen, Harri Kokkola, Tommi Bergman, Gunnar Myhre, et al. Biomass burning aerosols in most climate models are too absorbing. *Nature communications*, 12(1):277, 2021.

D Chand, R Wood, TL Anderson, SK Satheesh, and RJ Charlson. Satellite-derived direct radiative effect of aerosols dependent on cloud cover. *Nature Geoscience*, 2(3):181–184, 2009.

María-Luisa Chas-Amil, Eduardo García-Martínez, and Julia Touza. Iberian peninsula october 2017 wildfires: Burned area and population exposure in galicia (nw of spain). *International Journal of Disaster Risk Reduction*, 48:101623, 2020.

Paul J Crutzen and Meinrat O Andreae. Biomass burning in the tropics: Impact on atmospheric chemistry and biogeochemical cycles. *science*, 250(4988):1669–1678, 1990.

Ajinkya Desai, Clément Guilloteau, Warren E Heilman, Joseph J Charney, Nicholas S Skowronski, Kenneth L Clark, Michael R Gallagher, Efi Foufoula-Georgiou, and Tirtha Banerjee. Investigating fire–atmosphere interaction in a forest canopy using wavelets. *Boundary-Layer Meteorology*, 190(5):21, 2024.

Deutscher Wetterdienst. Deutscher wetterdienst. URL `https://www.dwd.de/EN/research/weatherforecasting/num_modelling/01_num_weather_prediction_modells/num_weather_prediction_models_node.html`.

Michael S Diamond, Pablo E Saide, Paquita Zuidema, Andrew S Ackerman, Sarah J Doherty, Ann M Fridlind, Hamish Gordon, Calvin Howes, Jan Kazil, Takanobu Yamaguchi, et al. Cloud adjustments from large-scale smoke-circulation interactions strongly modulate the southeast atlantic stratocumulus-to-cumulus transition. *Atmospheric Chemistry and Physics Discussions*, 2022:1–57, 2022.

Ke Ding, Xin Huang, Aijun Ding, Minghuai Wang, Hang Su, Veli-Matti Kerminen, Tuukka Petäjä, Zhemin Tan, Zilin Wang, Derong Zhou, et al. Aerosol-boundary-layer-monsoon interactions amplify semi-direct effect of biomass smoke on low cloud formation in southeast asia. *Nature communications*, 12(1):6416, 2021.

Lingyao Dong, Minghuai Wang, Daniel Rosenfeld, Yannian Zhu, Yuan Wang, Xinyi Dong, Zhoukun Liu, Hao Wang, Yi Zeng, Yang Cao, et al. Effects of smoke on marine low clouds and radiation during 2020 western united states wildfires. *Atmospheric Research*, 302: 107295, 2024.

AP Fernandes, D Lopes, S Sorte, A Monteiro, C Gama, J Reis, I Menezes, T Osswald, C Borrego, M Almeida, et al. Smoke emissions from the extreme wildfire events in central portugal in october 2017. *International Journal of Wildland Fire*, 31(11):989–1001, 2022.

Saulo R Freitas, Karla M Longo, Robert Chatfield, D Latham, Maria Assunção Faus da Silva Dias, MO Andreae, E Prins, JC Santos, R Gielow, and JA Carvalho Jr. Including the sub-grid scale plume rise of vegetation fires in low resolution atmospheric transport models. *Atmospheric Chemistry and Physics*, 7(13):3385–3398, 2007.

SR Freitas, KM Longo, and MO Andreae. Impact of including the plume rise of vegetation fires in numerical simulations of associated atmospheric pollutants. *Geophysical Research Letters*, 33(17), 2006.

Michael Fromm, Daniel T Lindsey, René Servranckx, Glenn Yue, Thomas Trickl, Robert Sica, Paul Doucet, and Sophie Godin-Beekmann. The untold story of pyrocumulonimbus. *Bulletin of the American Meteorological Society*, 91(9):1193–1210, 2010.

Almut Gassmann and Hans-Joachim Herzog. Towards a consistent numerical compressible non-hydrostatic model using generalized hamiltonian tools. *Quarterly Journal of the Royal Meteorological Society*, 134(635):1597–1613, 2008.

Marco A Giorgetta, Renate Brokopf, Traute Crueger, Monika Esch, Stephanie Fiedler, J Helmert, Cathy Hohenegger, Luis Kornblueh, M Köhler, Elisa Manzini, et al. Icon-a, the atmosphere component of the icon earth system model: I. model description. *Journal of Advances in Modeling Earth Systems*, 10(7):1613–1637, 2018.

Scott L Goodrick, Timothy J Brown, and W Matt Jolly. Weather, fuels, fire behavior, plumes, and smoke-the nexus of fire meteorology. *Fire Management Today.*, 75(1):33–38, 2017.

G Grell, SR Freitas, Martin Stuefer, and J Fast. Inclusion of biomass burning in wrf-chem: impact of wildfires on weather forecasts. *Atmospheric Chemistry and Physics*, 11(11): 5289–5303, 2011.

Marc Grünig, Rupert Seidl, and Cornelius Senf. Increasing aridity causes larger and more severe forest fires across europe. *Global Change Biology*, 29(6):1648–1659, 2023.

Marc Grünig, Werner Rammer, Cornelius Senf, Katharina Albrich, Frédéric André, Andrey LD Augustynczik, Martin Baumann, Friedrich J Bohn, Meike Bouwman, Harald Bugmann, et al. Climate change will increase forest disturbances in europe throughout the 21st century. *Science*, 391(6789):eadx6329, 2026.

Edward Gryspeerdt, Johannes Quaas, and Nicolas Bellouin. Constraining the aerosol influence on cloud fraction. *Journal of Geophysical Research: Atmospheres*, 121(7):3566–3583, 2016.

Michael Hess, Peter Koepke, and Ingrid Schult. Optical properties of aerosols and clouds: The software package opac. *Bulletin of the American meteorological society*, 79(5):831–844, 1998.

Robin J Hogan and Alessio Bozzo. A flexible and efficient radiation scheme for the ecmwf model. *Journal of Advances in Modeling Earth Systems*, 10(8):1990–2008, 2018.

Gholam Ali Hoshyaripour, Andreas Baer, Sascha Bierbauer, Julia Bruckert, Dominik Brunner, Jochen Foerstner, Arash Hamzehloo, Valentin Hanft, Corina Keller, Martina Klose, et al. The atmospheric composition component of the icon modeling framework: Icon-art version 2025.04. *EGUsphere*, 2025:1–54, 2025.

Gholam Ali Hoshyaripour, Andreas Baer, Sascha Bierbauer, Julia Bruckert, Dominik Brunner, Jochen Förstner, Arash Hamzehloo, Valentin Hanft, Corina Keller, Martina Klose, et al. The atmospheric composition component of the icon modeling framework: Icon-art version 2025.10. *Geoscientific Model Development*, 19(4):1645–1681, 2026.

Sha Huang, Lina Tang, Joseph P Hupy, Yang Wang, and Guofan Shao. A commentary review on the use of normalized difference vegetation index (ndvi) in the era of popular remote sensing. *Journal of forestry research*, 32(1):1–6, 2021.

Intergovernmental Panel on Climate Change (IPCC). *The Earth's Energy Budget, Climate Feedbacks and Climate Sensitivity*, pages 923–1054. Cambridge University Press, 2021. doi: 10.1017/9781009157896.009.

Joanna Joiner, Yasuko Yoshida, Martha Anderson, Thomas Holmes, Christopher Hain, Rolf Reichle, Randal Koster, Elizabeth Middleton, and Fan-Wei Zeng. Global relationships among traditional reflectance vegetation indices (ndvi and ndii), evapotranspiration (et), and soil moisture variability on weekly timescales. *Remote Sensing of Environment*, 219: 339–352, 2018.

JW Kaiser, A Heil, MO Andreae, A Benedetti, N Chubarova, L Jones, J-J Morcrette, M Razinger, MG Schultz, M Suttie, et al. Biomass burning emissions estimated with a global fire assimilation system based on observed fire radiative power. *Biogeosciences*, 9 (1):527–554, 2012.

Ziming Ke, Yuhang Wang, Yufei Zou, Yongjia Song, and Yongqiang Liu. Global wildfire plume-rise data set and parameterizations for climate model applications. *Journal of Geophysical Research: Atmospheres*, 126(6):e2020JD033085, 2021.

Man-Hae Kim, Ali H Omar, Jason L Tackett, Mark A Vaughan, David M Winker, Charles R Trepte, Yongxiang Hu, Zhaoyan Liu, Lamont R Poole, Michael C Pitts, et al. The calipso version 4 automated aerosol classification and lidar ratio selection algorithm. *Atmospheric measurement techniques*, 11(11):6107–6135, 2018.

D Koch and AD Del Genio. Black carbon semi-direct effects on cloud cover: review and synthesis. *Atmospheric Chemistry and Physics*, 10(16):7685–7696, 2010.

Daniel Leuenberger, Marcel Koller, Oliver Fuhrer, and Christoph Schär. A generalization of the sleve vertical coordinate. *Monthly Weather Review*, 138(9):3683–3689, 2010.

Rodman R Linn, John Kevin Hiers, Joseph J O'Brien, Kara Yedinak, Chad Hoffman, Jesse Canfield, David Robinson, and Scott Goodrick. Wildland fire entrainment: The missing link between wildland fire and its environment. *PNAS nexus*, 4(1):pgae576, 2025.

José María López-Romero, Juan Pedro Montávez, Sonia Jerez, Raquel Lorente-Plazas, Laura Palacios-Peña, and Pedro Jiménez-Guerrero. Precipitation response to aerosol–radiation and aerosol–cloud interactions in regional climate simulations over europe. *Atmospheric Chemistry and Physics*, 21(1):415–430, 2021.

Alexei Lyapustin, Yujie Wang, Sergey Korkin, and Dong Huang. Modis collection 6 maiac algorithm. *Atmospheric Measurement Techniques*, 11(10):5741–5765, 2018.

Alexei I Lyapustin, Yujie Wang, Istvan Laszlo, Thomas Hilker, Forrest G Hall, Piers J Sellers, Compton J Tucker, and Sergey V Korkin. Multi-angle implementation of atmospheric correction for modis (maiac): 3. atmospheric correction. *Remote Sensing of Environment*, 127:385–393, 2012.

Catarina Mansilha, Armindo Melo, Zita E Martins, Isabel MPLVO Ferreira, Ana Maria Pereira, and Jorge Espinha Marques. Wildfire effects on groundwater quality from springs connected to small public supply systems in a peri-urban forest area (braga region, nw portugal). *Water*, 12(4):1146, 2020.

Paul Moore. An analysis of storm ophelia which struck ireland on the 16th october 2017. Technical report, Met Éireann, Glasnevin Hill, Dublin 9, October 2018. URL `https://www.met.ie/cms/assets/uploads/2018/10/OpheliaReport.pdf`.

Lukas O Muser, Gholam Ali Hoshyaripour, Julia Bruckert, Ákos Horváth, Elizaveta Malinina, Sandra Wallis, Fred J Prata, Alexei Rozanov, Christian von Savigny, Heike Vogel, et al. Particle aging and aerosol–radiation interaction affect volcanic plume dispersion: evidence from the raikoke 2019 eruption. *Atmospheric Chemistry and Physics*, 20(23): 15015–15036, 2020.

Lisa Janina Muth. *Numerical Simulations of the Black Summer Fires: Impact of Moisture, Sensible Heat Release and Aerosol-Radiation Interaction on the Smoke Plume and Cloud Formation.* PhD thesis, Karlsruher Institut für Technologie (KIT), 2024.

Lisa Janina Muth, Sascha Bierbauer, Corinna Hoose, Bernhard Vogel, Heike Vogel, and Gholam Ali Hoshyaripour. Influence of fire-induced heat and moisture release on pyro-convective cloud dynamics during the australian new year's event: a study using convection-resolving simulations and satellite data. *Atmospheric Chemistry and Physics*, 25(22):16027–16040, 2025.

Declan O'Donnell. *Towards the assessment of the climate effects of secondary organic aerosols.* PhD thesis, Hamburg University Hamburg, 2010.

Kevin Ohneiser, Albert Ansmann, Jonas Witthuhn, Hartwig Deneke, Alexandra Chudnovsky, Gregor Walter, and Fabian Senf. Self-lofting of wildfire smoke in the troposphere and stratosphere: simulations and space lidar observations. *Atmospheric Chemistry and Physics*, 23(4):2901–2925, 2023.

Marta Oliveira, Cristina Delerue-Matos, Maria Carmo Pereira, and Simone Morais. Environmental particulate matter levels during 2017 large forest fires and megafires in the center region of portugal: A public health concern? *International journal of environmental research and public health*, 17(3):1032, 2020.

Ali H Omar, David M Winker, Mark A Vaughan, Yongxiang Hu, Charles R Trepte, Richard A Ferrare, Kam-Pui Lee, Chris A Hostetler, Chieko Kittaka, Raymond R Rogers, et al. The calipso automated aerosol classification and lidar ratio selection algorithm. *Journal of Atmospheric and Oceanic Technology*, 26(10):1994–2014, 2009.

Brett B Palm, Qiaoyun Peng, Carley D Fredrickson, Ben H Lee, Lauren A Garofalo, Matson A Pothier, Sonia M Kreidenweis, Delphine K Farmer, Rudra P Pokhrel, Yingjie Shen, et al. Quantification of organic aerosol and brown carbon evolution in fresh wildfire plumes. *Proceedings of the National Academy of Sciences*, 117(47):29469–29477, 2020.

Jagabandhu Panda, Ankan Sarkar, and Ram Kumar Giri. Atmospheric aerosols and their effects on radiation, clouds, and precipitation in different meteorological scenarios. *Vayumandal*, 49(1):50–87, 2023.

Ronan Paugam, Martin Wooster, Saulo Freitas, and M Val Martin. A review of approaches to estimate wildfire plume injection height within large-scale atmospheric chemical transport models. *Atmospheric Chemistry and Physics*, 16(2):907–925, 2016.

David A Peterson, James R Campbell, Edward J Hyer, Michael D Fromm, George P Kablick III, Joshua H Cossuth, and Matthew T DeLand. Wildfire-driven thunderstorms cause a volcano-like stratospheric injection of smoke. *NPJ climate and atmospheric science*, 1(1): 30, 2018.

Steven Platnick, Kerry G Meyer, Michael D King, Galina Wind, Nandana Amarasinghe, Benjamin Marchant, G Thomas Arnold, Zhibo Zhang, Paul A Hubanks, Robert E Holz, et al. The modis cloud optical and microphysical products: Collection 6 updates and examples from terra and aqua. *IEEE Transactions on Geoscience and Remote Sensing*, 55(1): 502–525, 2016.

Alexandre M Ramos, Ana Russo, Carlos C DaCamara, Silvia Nunes, Pedro Sousa, PMM Soares, Miguel M Lima, Alexandra Hurduc, and Ricardo M Trigo. The compound event that triggered the destructive fires of october 2017 in portugal. *Iscience*, 26(3), 2023.

JS Reid, R Koppmann, TF Eck, and DP Eleuterio. A review of biomass burning emissions part ii: intensive physical properties of biomass burning particles. *Atmospheric chemistry and physics*, 5(3):799–825, 2005.

Samuel Rémy, Andreas Veira, Ronan Paugam, Mikhail Sofiev, Johannes W Kaiser, Franco Marenco, Sharon P Burton, Angela Benedetti, Richard J Engelen, Richard Ferrare, et al. Two global data sets of daily fire emission injection heights since 2003. *Atmospheric Chemistry and Physics*, 17(4):2921–2942, 2017.

Daniel Rieger, M Bangert, I Bischoff-Gauss, J Förstner, K Lundgren, D Reinert, J Schröter, H Vogel, G Zängl, R Ruhnke, et al. Icon-art 1.0–a new online-coupled model system from the global to regional scale. *Geoscientific Model Development Discussions*, 8(1):567–614, 2015.

Jaume Ruiz de Morales, Josep Calbó, Josep-Abel González, Hendrik Andersen, Jan Cermak, Julia Fuchs, and Yolanda Sola. Global assessment of the cloud-aerosol transition zone using calipso. *Advances in Atmospheric Sciences*, 43(2):321–335, 2026.

Bjørn H Samset, Camilla W Stjern, Elisabeth Andrews, Ralph A Kahn, Gunnar Myhre, Michael Schulz, and Gregory L Schuster. Aerosol absorption: Progress towards global and regional constraints. *Current climate change reports*, 4(2):65–83, 2018.

Jennifer Schröter, Daniel Rieger, Christian Stassen, Heike Vogel, Michael Weimer, Sven Werchner, Jochen Förstner, Florian Prill, Daniel Reinert, Günther Zängl, et al. Icon-art 2.1: A flexible tracer framework and its application for composition studies in numerical weather forecasting and climate simulations. *Geoscientific Model Development*, 11(10): 4043–4068, 2018.

CJ Smith, RJ Kramer, G Myhre, PM Forster, BJ Soden, T Andrews, Olivier Boucher, G Faluvegi, Dagmar Fläschner, Ø Hodnebrog, et al. Understanding rapid adjustments to diverse forcing agents. *Geophysical Research Letters*, 45(21):12–023, 2018.

Andrew Staniforth and John Thuburn. Horizontal grids for global weather and climate prediction models: a review. *Quarterly Journal of the Royal Meteorological Society*, 138 (662):1–26, 2012.

Philip Stier. Limitations of passive remote sensing to constrain global cloud condensation nuclei. *Atmospheric Chemistry and Physics*, 16(10):6595–6607, 2016.

Ina Tegen and Bernd Heinold. Large-scale modeling of absorbing aerosols and their semi-direct effects. *Atmosphere*, 9(10):380, 2018.

Christiane Textor, M Schulz, S Guibert, Stefan Kinne, Yves Balkanski, S Bauer, T Berntsen, T Berglen, Olivier Boucher, M Chin, et al. Analysis and quantification of the diversities of aerosol life cycles within aerocom. *Atmospheric Chemistry and Physics*, 6(7):1777–1813, 2006.

Marco Turco, Sonia Jerez, Sofia Augusto, Patricia Tarín-Carrasco, Nuno Ratola, Pedro Jiménez-Guerrero, and Ricardo M Trigo. Climate drivers of the 2017 devastating fires in portugal. *Scientific reports*, 9(1):13886, 2019.

CW Turner. Persistency of fat secretion during the lactation period as affected by age. *Journal of Dairy Science*, 10(2):95–105, 1927.

SJAE Twomey. Pollution and the planetary albedo. *Atmospheric Environment (1967)*, 8(12): 1251–1256, 1974.

Maria Val Martin, Ralph A Kahn, Jennifer A Logan, Ronan Paugam, Martin Wooster, and Charles Ichoku. Space-based observational constraints for 1-d fire smoke plume-rise models. *Journal of Geophysical Research: Atmospheres*, 117(D22), 2012.

Mark A Vaughan, Kathleen A Powell, David M Winker, Chris A Hostetler, Ralph E Kuehn, William H Hunt, Brian J Getzewich, Stuart A Young, Zhaoyan Liu, and Matthew J McGill. Fully automated detection of cloud and aerosol layers in the calipso lidar measurements. *Journal of Atmospheric and Oceanic Technology*, 26(10):2034–2050, 2009.

Carolin Walter, Saulo R Freitas, Christoph Kottmeier, Isabel Kraut, Daniel Rieger, Heike Vogel, and Bernhard Vogel. The importance of plume rise on the concentrations and atmospheric impacts of biomass burning aerosol. *Atmospheric Chemistry and Physics*, 16 (14):9201–9219, 2016.

Michael Weimer, Jennifer Schröter, Johannes Eckstein, Konrad Deetz, Marco Neumaier, Garlich Fischbeck, Lu Hu, Dylan B Millet, Daniel Rieger, Heike Vogel, et al. An emission module for icon-art 2.0: implementation and simulations of acetone. *Geoscientific Model Development*, 10(6):2471, 2017.

David M Winker, Mark A Vaughan, Ali Omar, Yongxiang Hu, Kathleen A Powell, Zhaoyan Liu, William H Hunt, and Stuart A Young. Overview of the calipso mission and caliop data processing algorithms. *Journal of Atmospheric and Oceanic Technology*, 26(11):2310–2323, 2009.

Kevin P Wyche, Hugo Ricketts, Mathew Brolly, and Kirsty L Smallbone. Emerging investigator series: the red sky: investigating the hurricane ophelia saharan dust and biomass burning aerosol event. *Environmental Science: Atmospheres*, 2(2):165–181, 2022.

Günther Zängl, Daniel Reinert, Pilar Rípodas, and Michael Baldauf. The icon (icosahedral non-hydrostatic) modelling framework of dwd and mpi-m: Description of the non-hydrostatic dynamical core. *Quarterly Journal of the Royal Meteorological Society*, 141 (687):563–579, 2015.

Victor M Zavala, Emil M Constantinescu, Theodore Krause, and Mihai Anitescu. On-line economic optimization of energy systems using weather forecast information. *Journal of Process Control*, 19(10):1725–1736, 2009.

Wilford Zdunkowski and Andreas Bott. *Dynamics of the atmosphere: a course in theoretical meteorology*. Cambridge University Press, 2003.

Charlie Zender. Particle size distributions: theory and application to aerosols, clouds, and soils, 2008.

Acknowledgments

I would like to sincerely thank my supervisor, Prof. Dr. Jan Cermak, for giving me the opportunity to conduct this research and to be part of his research group.

I would like to thank Dr. Gholamali Hoshyaripour for his support and helpful discussions during this work. His insights were valuable for the development of this study.

I am especially grateful to Dr. Eva Pauli for her valuable comments and suggestions. She has been a continuous source of inspiration and has always supported me whenever help was needed.

Special thanks also goes to Tabea Unser for her constant emotional support, encouragement with helpful discussions, valuable ideas, and constructive feedback, which greatly contributed to improving this study.

I would also thank the following individuals for their support throughout my thesis: Dr. Hendrik Andersen and Dr. Lisa Muth for their wonderful ideas that directly impacted how i conducted my research, Dr. Alexandre Ramos who helped me to fully understand the 2017 wildfire event and Dr. Katerina Kusakova for her emotional support and facilitating my acquaintance with the topic.

Utmost gratitude to all colleagues from the HiWi room and the members of Dr. Hoshyaripour's research group for creating such a friendly and supportive working environment and welcoming me so warmly in their group.

Last but not least, I would like to express my deepest gratitude to my family and friends who put up with me during my studies and especially my best friend and husband, Yohanna. Your constant support, encouragement, and belief in me gave me the strength and motivation to complete this journey. I cannot fully express how grateful I am to have you in my life.